

# The peculiar chemical abundance of the transitional millisecond pulsar PSR J1023+0038 - Li enhancement

T. Shahbaz,<sup>1,2\*</sup> J. I. González-Hernández,<sup>1,2</sup> R. P. Breton,<sup>3</sup> M. R. Kennedy,<sup>4,3</sup> D. Mata Sánchez<sup>1,2</sup> and M. Linares<sup>5,6</sup>

<sup>1</sup>*Instituto de Astrofísica de Canarias (IAC), E-38200 La Laguna, Tenerife, Spain*

<sup>2</sup>*Departamento de Astrofísica, Universidad de La Laguna (ULL), E-38206 La Laguna, Tenerife, Spain*

<sup>3</sup>*Jodrell Bank Centre for Astrophysics, School of Physics and Astronomy, The University of Manchester, Manchester M13 9PL, UK*

<sup>4</sup>*Department of Physics, University College Cork, Cork, Ireland*

<sup>5</sup>*Institutt for Fysikk, Norwegian University of Science and Technology, Trondheim, Norway*

<sup>6</sup>*Departament de Física, EEBE, Universitat Politècnica de Catalunya, Av. Eduard Maristany 16, E-08019 Barcelona, Spain*

Accepted XXX. Received YYY; in original form ZZZ

## ABSTRACT

Using high-resolution optical spectroscopy we determine the chemical abundance of the secondary star in the binary millisecond pulsar PSR J1023+0038. We measure a metallicity of  $[\text{Fe}/\text{H}] = 0.48 \pm 0.04$  which is higher than the Solar value and in general find that the element abundances are different compared to the secondary stars in X-ray binaries and stars in the solar neighbourhood of similar Fe content. Our results suggest that the pulsar was formed in a supernova explosion. We find that supernova models, where matter that has been processed in the supernova is captured by the secondary star leading to abundance anomalies, qualitatively agree with the observations. We measure Li abundance of  $A(\text{Li}) = 3.66 \pm 0.20$ , which is anomalously high compared to the Li abundance of stars with the same effective temperature, irrespective of the age of the system. Furthermore, the Li abundance in PSR J1023+0038 is higher than the Cosmic value and what is observed in young Population I stars and so provides unambiguous evidence for fresh Li production. The most likely explanation is the interaction of high energy gamma-rays or relativistic protons from the pulsar wind or intrabinary shock with the CNO nuclei in the secondary star's atmosphere via spallation which leads to substantial Li enrichment in the secondary star's atmosphere.

**Key words:** binaries: close, stars: fundamental parameters, stars: neutron, X-rays: binaries, stars: individual: PSR J1023+0038, pulsars: individual: PSR J1023+0038

## 1 INTRODUCTION

It is generally accepted that binary millisecond pulsars (MSPs) are produced via a recycling scenario which follows the evolution of low-mass X-ray binaries (LMXBs) containing a slowly rotating neutron star. In these systems a phase of heavy mass accretion from an evolving, non-degenerate, Roche Lobe filling secondary star eventually spun up the pulsar to millisecond spin periods (Alpar et al. 1982; Radhakrishnan & Srinivasan 1982; Bhattacharya & van den Heuvel 1991). MSPs can also be formed by accretion-induced collapse of massive white dwarfs (Smedley et al. 2015). By accreting material from the secondary star, the white dwarf increases its mass above the Chandrasekhar mass limit and electron capture leads to collapse of the white dwarf, resulting in a low-field, rapidly rotating neutron star (Nomoto & Kondo 1991; Ferrario & Wickramasinghe 2007). Indeed, Hurley et al. (2010) investigated formation rates of accretion-induced collapse neutron stars using population synthesis methods and found that accretion-induced collapse systems provide a complementary important contribution to the formation pathway to MSPs than recycling.

Binary MSPs are divided into classes according to the nature of their secondary star, which can be either a degenerate or a non-degenerate object. The ‘redback’ class have relatively massive  $>0.2 M_{\odot}$ , non-degenerate secondary stars, whereas the ‘black widow’ class contain semi-degenerate  $<0.1 M_{\odot}$  low-mass secondary stars which have suffered significant mass-loss and ablation from the pulsar wind (Roberts 2013). Finally there are MSPs with degenerate, extremely low-mass ( $<0.3 M_{\odot}$ ) helium-core white dwarf companions (Brown et al. 2013). Currently there is a population of 22 redbacks (Linares & Kachelrieß 2021) of which 3 (at the time of writing) are transitional MSPs, switching between distinct states of accretion-powered and rotation-powered emission on time-scales of years. Indeed, the transitional MSPs have provided support for the recycling scenario (Archibald et al. 2009; Papitto et al. 2013; Bassa et al. 2014; Stappers et al. 2014; Patruno et al. 2014). For a full review of the transitional MSPs see Campana & Di Salvo (2018). It is thought that irradiation feedback (Benvenuto et al. 2014) and thermal-viscous instability in the accretion disc (Jia & Li 2015) is responsible for the transitions between the two states. X-rays absorbed by the secondary star produce a partial blockage of the energy arising from the star's interior leading to cyclic mass-transfer episodes between the X-ray

\* E-mail: tsh@iac.es

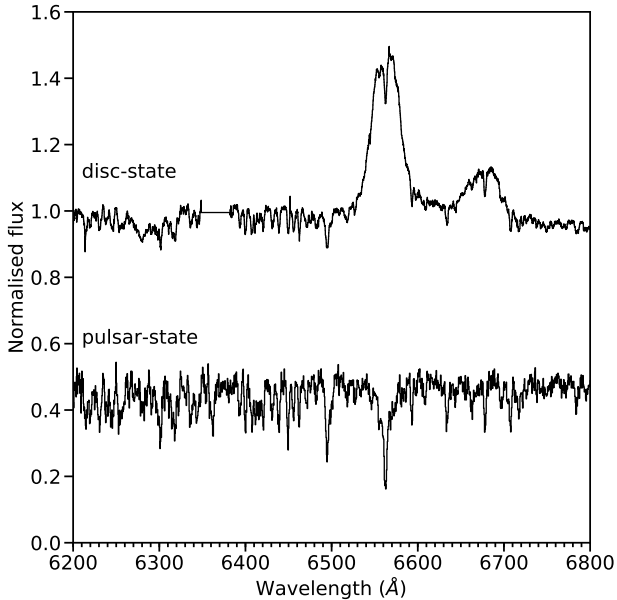


**Figure 1.** The 2009 pulsar-state spectrum (bottom) and 2016 disc-state spectrum (bottom), shifted vertically for clarity. The disc-state spectrum contains a gap between 6350–6400 Å due to bad columns in the CCD. Only part of the spectra are shown.

binary and radio pulsar states (Bünning & Ritter 2004; Benvenuto et al. 2014).

In the rotation-powered pulsar-state (PS) regular radio eclipses and pulsations are observed (Archibald et al. 2009, 2013). The stripping of mass from the companion as a result of bombardment by the energetic wind of the MSP causes the companion star to bloat and is the favoured mass-loss mechanism (Ruderman et al. 1989). This mass-loss gives rise to long eclipses at superior conjunction, often covering most of the orbit (Polzin et al. 2018, 2020). The optical light curves show an asymmetric single-humped modulation, due to the combined effects of the nearly Roche lobe filling tidally-locked secondary star’s ellipsoidal modulation and the high-energy emission from the pulsar wind heating of the inner face of the secondary star (Breton et al. 2013; Schroeder & Halpern 2014; Strader et al. 2019). In multiple systems, the asymmetric light curves suggests that the heating does not come directly from the isotropic pulsar wind, but is due to non-thermal X-ray emission produced by the intrabinary shock between the pulsar and secondary star’s wind (Romani & Sanchez 2016), or gets redistributed around the star (Kandel et al. 2019; Voisin et al. 2020).

In the accretion-powered disc-state (DS), no radio pulsations are detected and the system is much brighter at optical and X-ray wavelengths due to the presence of an accretion disc. X-ray pulsations at the neutron star spin period are observed (Archibald et al. 2009). The secondary star is close to fully filling its Roche lobe and the accretion disc is observed via broad emission lines. The optical light curve is similar to that in the pulsar-state suggesting that the level of irradiation/heating of the secondary star is similar (Kennedy et al. 2018). The effects of heating are observed in the optical spectra (Shahbaz et al. 2019) but it is not clear if the source of the irradiation is the high-energy emission from the pulsar relativistic wind or the X-ray emission from inner regions of the accretion disc. Low- and high-mode flux variations (Bogdanov et al. 2015; Shahbaz et al. 2015) and coherent optical and X-ray pulsations are observed

(Ambrosino et al. 2017; Archibald et al. 2015) as well as GeV emission (Takata et al. 2014; Papitto et al. 2019). Recently, two similar models have been proposed to explain the properties observed in PSR J1023+0038 (Veledina et al. 2019; Papitto et al. 2019); the dissipative collision between a rotating striped pulsar wind at a few light cylinder radii away from the pulsar, gives rise synchrotron emission producing the optical and X-ray pulses.

The observed properties of binary MSPs depend on their evolutionary path. Indeed, the way in which the neutron star is formed, the mass of the donor star and the orbital separation after the birth of the neutron star, dictates the evolutionary state of the system. It is generally believed that in a binary consisting of a massive star and a low-mass donor star, mass transfer will become dynamically unstable and the binary undergoes a phase of common envelope evolution. During this phase the donor star spirals in towards the centre of the massive star ( $>10 M_{\odot}$ ) ejecting most of its envelope, leaving behind a naked He-burning core. A neutron star is subsequently born after the explosion of the helium star. If the binary is not disrupted and if the orbital separation is small enough, the (evolved) non-degenerate donor star fills its Roche lobe and the binary undergoes a subsequent epoch of mass transfer on to the neutron star. In this phase the system is observed as an X-ray binary (Tauris & van den Heuvel 2006).

The donor star is expected to lose a significant amount of its outermost layers, a small fraction of which is accreted by the neutron star. In a strongly peeled star, we observe the chemical composition that has been previously modified by thermonuclear reactions. In material partially processed by the CNO cycle, C depletion and N enhancement is expected (Chen et al. 2013). It is also possible that the SN explosion producing the neutron star modifies the chemistry of the donor star. The chemical abundances of the donor/secondary star in black hole and neutron star X-ray binaries has been studied in several systems: Nova Scorpii 1994 (Israelian et al. 1999a; González Hernández et al. 2008a), A0620-00 (González Hernández et al. 2004), Cen X-4 (González Hernández et al. 2005), XTE J1118+480 (González Hernández et al. 2006, 2008c), Cyg X-2 (Suárez-Andrés et al. 2015a), V404 Cyg (González Hernández et al. 2011), and V4641 Sgr (Orosz et al. 2001; Sadakane et al. 2006), taking into account different scenarios of pollution from supernova (SN) or hypernova (HN) ejecta. The chemical abundances of secondary stars show over-abundance of several  $\alpha$ -elements (such as O, S, Si) which has been interpreted as pollution by matter ejected during the SN (see González Hernández et al. 2011, and references within).

The only MSP where a spectroscopic chemical abundance analysis exists is for PSR J1740–5340, which lies in the globular cluster NGC 6397 (D’Amico et al. 2001). PSR J1740–5340 is a redback MSP which has a non-degenerate secondary star ( $\sim 0.3 M_{\odot}$ ) in a 32.5 hr binary orbit (Ferraro et al. 2001; Orosz & van Kerkwijk 2003). Anomalous Li, Ca and C abundances are observed and a comparison with theoretical models indicates that the companion is the low-mass remnant star of a deeply peeled  $0.8 M_{\odot}$  progenitor (Mucciarelli et al. 2013). In this paper we use high-resolution spectra to derive the stellar parameters and chemical abundances of the secondary star in the binary MSP PSR J1023+0038. We compare the abundances with stars in the Solar neighbourhood as well as the secondary stars in X-ray binaries. We also compare the determined abundances in the context of enrichment of the secondary star from SN/HN yields as well as CNO evolution models. Finally we investigate the viability of various Li enrichment scenarios via spallation of the CNO nuclei in the atmosphere of the secondary star.

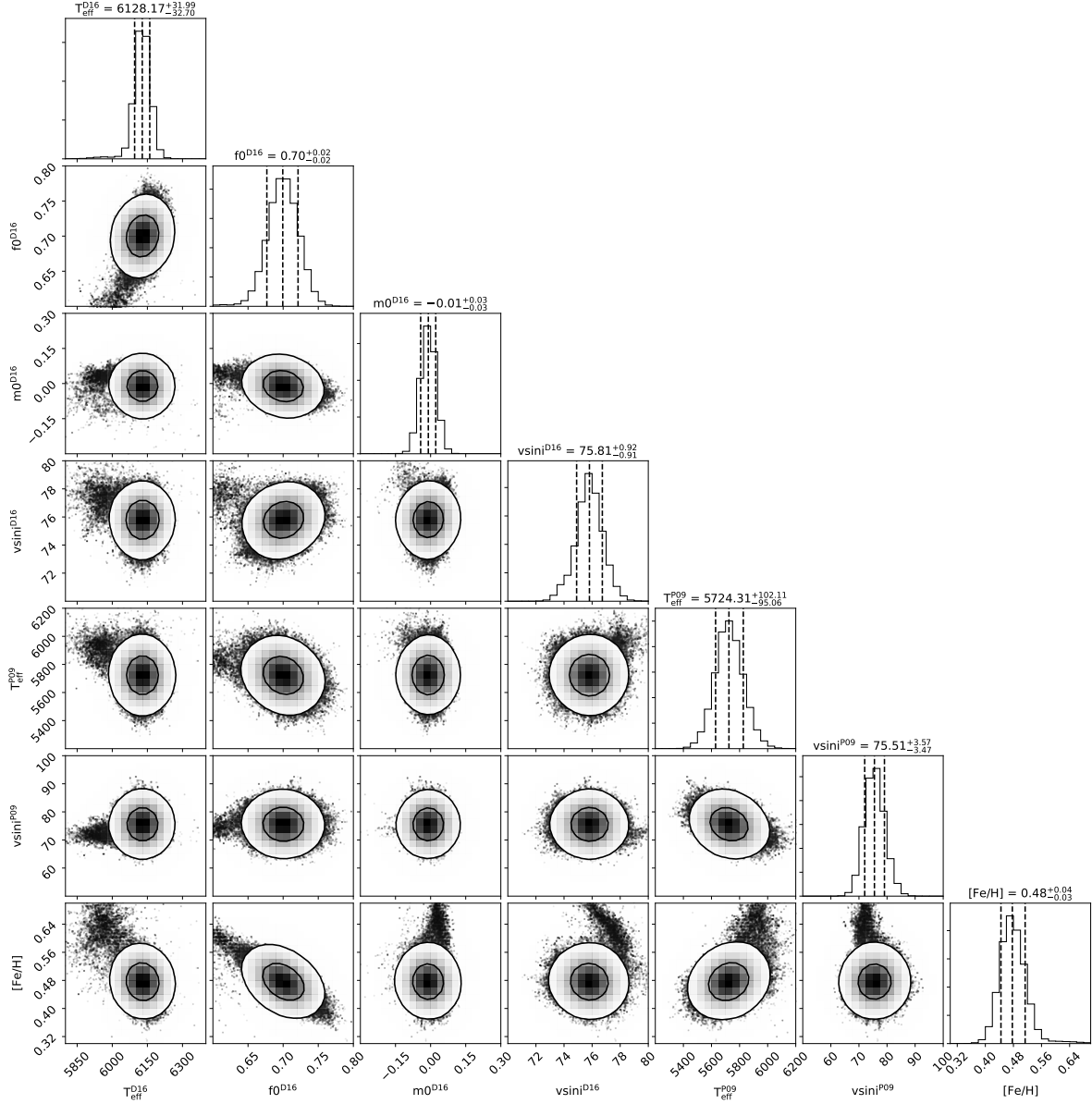


**Figure 2.** MCMC 2-D model parameter distributions resulting from synthetic fits to the observed spectrum of PSR J1023+0038 to determine the stellar parameters. The contours in the 2-D plots show the 1 and 2 sigma confidence regions, and the projected 1-D parameter distributions with the mean and standard deviation. The superscript D16 and D09 refer to the 2016 disc-state (D16) and 2009 pulsar-state (P09), respectively.

**Table 1.** The results of the MCMC analysis to determine the stellar parameters of PSR J1023+0038.

Parameter	pulsar-state 2009	disc-state 2016
$T_{\text{eff}}$ (K)	$5724^{+102}_{-95}$	$6128^{+32}_{-33}$
$v_{\text{rot}} \sin i$ (km s $^{-1}$ )	$75.5^{+3.6}_{-3.5}$	$75.8^{+0.9}_{-0.9}$
$f_0$	1.0	$0.70^{+0.02}_{-0.02}$
$m_0 \times 10^{-3}$	0.0	$-0.01^{+0.03}_{-0.03}$

## 2 CHEMICAL ANALYSIS

The spectra analysed here have been presented in [Shahbaz et al. \(2019\)](#) and so we refer the reader to it for the data reduction de-

tails. The pulsar-state spectrum covers spectral range 6200–6900 Å with velocity resolution of 24 km s $^{-1}$  whereas the disc-state spectrum covers 5300–10200 Å with a velocity resolution of 40 km s $^{-1}$ . The disc-state spectra clearly show broad Balmer and He lines emission lines related to the presence of an accretion disc. The spectral range 6200–6900 Å is common to both the pulsar- and disc-state spectra. Both data sets cover the full orbital phase range, have been Doppler-corrected to the secondary star’s rest frame ([Shahbaz et al. 2019](#)) and carefully normalized using a low-order spline fit to the continuum level (see Fig. 1).

### 2.1 Stellar Parameters

The chemical abundance of various elements in the secondary stars of X-ray binaries have been determined (see [González Hernández](#)

**Table 2.** LTE element abundances determined for PSR J1023+0038.

Element	$\log \epsilon(X)_{\odot}^a$	[X/Fe]	[X/H] <sup>b</sup>	A(X) <sup>c</sup>
Li <sup>d</sup>	3.31 <sup>f</sup>	0.02 ± 0.20	0.50 ± 0.20	3.66 ± 0.20
O <sup>d</sup>	8.74 <sup>e</sup>	-1.12 ± 0.10	-0.64 ± 0.11	8.10 ± 0.11
Al	6.47	0.87 ± 0.08	1.35 ± 0.09	7.82 ± 0.09
Si	7.55	0.02 ± 0.05	0.50 ± 0.06	8.05 ± 0.06
Ca	6.36	0.14 ± 0.05	0.62 ± 0.06	6.98 ± 0.06
Fe	7.50		0.48 ± 0.04	7.98 ± 0.04
Ni	6.25	0.47 ± 0.23	0.95 ± 0.24	7.20 ± 0.23

<sup>a</sup>Photospheric Solar abundances adopted from [Grevesse et al. \(1996\)](#).

<sup>b</sup> $[X/H] = \log[N(X)/N(H)] - \log[N(X)/N(H)]_{\odot}$ , where  $N(X)$  is the number density of atoms.

<sup>c</sup>Abundance expressed as  $A(X) = \log[N(X)/N(H)] + 12$ .

<sup>d</sup>Corrected for NLTE effects.

<sup>e</sup>Solar abundance from [Ecuivillon et al. \(2006\)](#).

<sup>f</sup>Meteoritic Solar abundance from [Grevesse et al. \(1996\)](#).

[et al. 2011](#), and references within). We use a similar method to perform a chemical abundance analysis of the secondary star in PSR J1023+0038 in the pulsar- and disc-state. We simultaneously fit the 2009 pulsar- and 2016 disc-state spectra with a synthetic model to first determine the stellar parameters and then determine the chemical abundance of the secondary star in each state.

We determine the stellar parameters, effective temperature  $T_{\text{eff}}$ , surface gravity  $\log g$  and the [Fe/H] metallicity, using synthetic spectral fits to the observed spectra. To compute the synthetic spectra we use the 2014 version of the 1D local thermodynamic equilibrium (LTE) code MOOG version 2013<sup>1</sup> ([Snedden et al. 2012](#)). We use the atomic line data from the Vienna Atomic Line Database VALD-2;<sup>2</sup> ([Kupka et al. 2000](#)) and a grid of local thermodynamic equilibrium (LTE) model atmospheres provided by [Kurucz \(1993\)](#). The model grid spans  $T_{\text{eff}} = 5000\text{--}7000$  K in steps of 100 K,  $\log g = 3.0\text{--}5.0$   $\text{cm s}^{-2}$  in steps of 0.1 dex and [Fe/H] abundances between  $-0.5$  and  $1.0$  in steps of 0.1 dex. The micro-turbulence is computed using the expression which depends on effective temperature and surface gravity ([Adibekyan et al. 2012](#)). Subsequently, for a given model atmosphere we compute the synthetic spectra using MOOG.

It should be noted that in reality the secondary star is not spherical but has the shape of on star's Roche lobe (see e.g. [Shahbaz 1998](#)). In principle one should compute the orbital phase averaged spectrum taking into account the varying temperature and gravity across the secondary star's Roche lobe (mainly due to the gravity darkening, inclination angle) by incorporating synthetic spectra into the secondary star's Roche geometry. However, it has been shown that phase averaging smooths out the effects of the phase-dependant Roche lobe rotation profile, and so the phase averaged spectrum can be modelled by the spectrum of a single temperature star convolved with the Gray rotation profile ([González Hernández et al. 2008b](#)). Furthermore, it has been shown that LTE model atmospheres adequately describe the atmospheres of highly irradiated companions in black widow MSPs, suggesting that the energy from the pulsar is being deposited deep enough within the companion such that the surface radiates as a black body in LTE ([Kennedy et al. 2022](#)). Hence in the case of black widow MSP systems, these models are perfectly acceptable for modelling the secondary star.

We identify moderately strong, relatively isolated lines of several elements in the high-resolution solar flux atlas of ([Kurucz et al.](#)

[1984](#)). We then inspect the spectrum of PSR J1023+0038 and select several spectral features containing Fe I and Ca I with excitation potentials between 1 and 5 eV. We determine the synthetic spectrum for a given  $T_{\text{eff}}$ ,  $\log g$ , [Fe/H] combination and calculate the corresponding model atmosphere by interpolating the model atmosphere grid. Given that some of the Fe lines in our spectral range may be blended with Ca lines we also allow the [Ca/Fe] abundance to vary as a free parameter between  $-1.0$  and  $+1.0$  dex. Note that the final determination of Ca abundance is done once the stellar parameters have been determined (see Section 2.2). We also broaden the synthetic spectrum using the Gray rotation profile ([Gray 1992](#)) with a linear limb darkening coefficient of 0.63, appropriate for a  $\sim 60V$  star ([Al-Naimiy 1978](#)). Finally, before computing the  $\chi^2$  between the target and model spectrum, we degrade the synthetic spectrum using a Gaussian instrumental profile and then bin the synthetic spectrum to the same velocity scale as the target spectrum. To allow for the effects of a wavelength-dependent veiling caused by the presence of extra light in the system e.g. from an accretion disc ([Linares 2014](#); [Shahbaz et al. 2019](#)) or intrabinary shock ([Romani & Sanchez 2016](#)), we subtract a scaled version of the synthetic spectrum from the observed spectrum. We model this wavelength-dependent scale factor as a linear function, where the  $f_{6000}$  represents the fractional contribution of the secondary star to the observed spectrum at 6000 Å and the gradient is given by  $m_0$ . The parameters  $f_{6000}$  and  $m_0$  range from 0.1 to 1.0 and  $-0.5 \times 10^{-3}$  to  $+0.5 \times 10^{-3}$  Å<sup>-1</sup>, respectively.

We use five small spectral regions with a width of 20 Å centred on 6228 Å, 6435 Å and 6726 Å for the pulsar-state spectra and 6140 Å, 6222 Å, 6435 Å, 6745 Å and 7749 Å for the disc-state spectra regions devoid of emission lines (see Fig. 3). The model free parameters for each state are therefore,  $T_{\text{eff}}$ ,  $\log g$ ,  $f_{6000}$ ,  $m_0$ , [Fe/H], [Ca/Fe] and a wavelength shift (to allow for any possible shift between the observed and model spectrum).

The surface gravity of the secondary star is determined by its mass ( $M_2$ ) and radius ( $R_2$ ) as  $\log g = 4.438 + \log M_2 - 2 \log R_2$ . We can express  $R_2$  in terms of the star's equivalent volume radius ([Eggleton 1983](#))  $r_{\text{eqv}}$  (in units of the binary separation,  $a$ ), which depends on the binary mass and Roche lobe filling factor,  $f$  ([Shahbaz et al. 2017](#)). Given that  $M_2 = qM_1$  and  $a = 4.207M_1^{1/3} (1+q)^{1/3} P_{\text{orb}}^{2/3} R_{\odot}$ , the star's gravity can be expressed as

$$\log g = 4.438 + q \log M_1 - 2 \log a - 2 \log r_{\text{eqv}}(f, q) \quad (1)$$

Using  $q = 0.137$  ([Shahbaz et al. 2019](#)) and the expected limits on  $M_1 = 1.4\text{--}3.0 M_{\odot}$  (from a canonical to the maximum neutron star mass), we find that in the disc-state ( $f = 1$ ),  $\log g^{\text{DS}}$  is expected to lie in the range 4.57 to 4.68. Note that in the pulsar-state the secondary star may slightly underfill its Roche lobe ([Stringer et al. 2021](#)), but should be close to unity in the disc-state (because an accretion disc is observed). This means that the radius of the secondary star is smaller in the pulsar-state compared to the disc-state. We can therefore impose the following conditions: (1) the secondary star's rotational broadening in the disc-state is larger than the star's rotational broadening in the pulsar-state, (2)  $\log g$  in the pulsar-state is larger than  $\log g$  in the disc-state and (3)  $\log g$  in the disc-state lies in the range 4.57 to 4.68.

We perform the spectral fitting with the Markov-chain Monte Carlo (MCMC) package EMCEE ([Foreman-Mackey et al. 2013](#)), using the  $\chi^2$  minimization method and assuming flat priors. A total of 50 walkers were used with 5000 samples taken and a burn-in of 100 samples. From our preliminary fits we find that  $f_{6000}=1$  is required for the pulsar-state spectra. For speed, we therefore repeat the MCMC fits but fixing  $f_{6000}=1$  for the pulsar-state spectrum. For both the disc- and pulsar-state spectrum we find that we cannot constrain the gravity

<sup>1</sup> <https://www.as.utexas.edu/~chris/moog.html>

<sup>2</sup> <http://www.astro.univie.ac.at/~vald>

of the secondary star. In Fig. 2 we show the resulting relevant MCMC 2-D model parameter distributions. Inspection of the posteriors of the parameters do not show any obvious correlations between the parameters, and the individual parameter distributions follow normal distributions. The most likely values for the constrained parameters are given in Table 1. The sections of the disc- and pulsar-state spectrum along with the best model fit is shown in Fig. 3.

As a test we also perform the same analysis on a template field star taken from our UVES Paranal Observatory Project (Bagnulo et al. 2003) library of high signal-to-noise template spectra (Shahbaz et al. 2019). We rotationally broaden the template star spectrum HD 115617 by  $78 \text{ km s}^{-1}$ . We then degrade the template star spectrum to match the same spectral resolution and heliocentric velocity scale as the target spectrum in the pulsar- and disc-state. Finally we determine the stellar parameters using the same method and spectral regions as the target spectrum. We obtain the stellar parameters  $T_{\text{eff}} = 5470 \text{ K}$ ,  $\log g = 4.5 \text{ cm s}^{-2}$  and  $[\text{Fe}/\text{H}] = 0.06 \text{ dex}$  which are consistent with the observed value in the SIMBAD database (Wenger et al. 2000).

## 2.2 Stellar Abundances

Using the derived stellar parameters we identify several spectral regions containing various lines of O, Al, Si, Ca, Ni and Li, some of which are blended with Fe lines. We determine the abundances of these elements by comparing the observed pulsar- and disc-state spectra with modified versions of synthetic spectra computed using the best model atmosphere calculated with the corresponding stellar parameters and metallicity determined in Section 2.1. Again, before comparison we rotationally broaden and degrade the model spectrum to the same velocity scale as the target spectrum. We perform an MCMC spectral analysis (Foreman-Mackey et al. 2013) using the  $\chi^2$  minimization method and assume Gaussian priors for the corresponding stellar parameters and metallicity, and flat priors for the element abundances. The abundance  $[\text{X}/\text{H}]$  was allowed to vary between -2.0 and 2.0 dex. The Ca (see Figs. 4a and 4b) and Si (see Figs. 4c and 4d) abundances are derived from several lines in the spectral region 6425–6470 Å and 6235–6260 Å, respectively in both the disc- and pulsar-state spectra. Given the presence of H and He emission lines from the accretion disc in the disc-state, the Al and Li abundances are determined only from the pulsar-state spectrum by simultaneously fitting the Al I 6696 Å and Li I 6708 Å doublets (see Fig. 4e). In Fig. 5 we show both the pulsar- and disc-state spectra, where the contamination from the broad He II 6678.149 Å emission can be clearly seen in the disc-state spectrum.

The O and Ni abundances are derived using the O I 7771 Å triplet and Ni I 7790 Å lines, respectively, and are fitted simultaneously using the disc-state spectrum only, as the pulsar-state spectrum do not cover this spectral range (see Fig. 4f). The results of the MCMC analysis are shown in Fig. 6. We also perform the same analysis on the template star spectrum and the corresponding plots are shown in Fig. 4. The abundances determined for the various elements are given in Table 2. In Fig. 7 we show the abundances of the secondary star in PSR J1023+0038 in comparison with the abundances in G and K metal-rich dwarf stars (Adibekyan et al. 2012; Ecuivillon et al. 2006).

## 3 RESULTS

### 3.1 Stellar parameters

The light curves taken when PSR J1023+0038 was in the pulsar- (Woudt et al. 2004; Thorstensen & Armstrong 2005) and disc-state (Bogdanov et al. 2014; Shahbaz et al. 2015) show an asymmetric single-humped modulation. In the pulsar-state this is due to the combined effects of the tidally-locked secondary star’s ellipsoidal modulation and the high-energy emission from the pulsar’s relativistic wind powered by the rotational spin down of the neutron star heating the inner face of the secondary star. In the disc-state, as well as the star’s ellipsoidal modulation, the observed X-ray and gamma-ray luminosity (most likely due to accretion) is sufficient to provide the observed irradiating luminosity. Irradiation also has a pronounced effect on the phase-resolved spectra, where spectral type changes along the orbit have been observed (Shahbaz et al. 2019). The pulsar- to disc-state transition involves an increase in the gamma-ray and X-ray flux of a factor of  $\sim 20$  (Patruno et al. 2014; Takata et al. 2014), which implies that during the disc-state the secondary star is subject to irradiation from the accretion disc.

We determine the global temperature of the secondary star in the disc- and pulsar-state to be  $T_{\text{eff}}^{\text{PS}} = 5724 \text{ K}$  and  $T_{\text{eff}}^{\text{DS}} = 6128 \text{ K}$ , respectively, which correspond to spectral types of  $\sim \text{G1}$  and  $\text{F8}$ , respectively (Pecaut & Mamajek 2013). The transition from the pulsar- to disc-state results in a significant ( $3.8\text{-}\sigma$  level) increase in temperature, caused by the increased gamma-ray and X-ray flux. In contrast, from Kepler photometry Kennedy et al. 2018 find that the heating amplitude does change between states. However, it should be noted that absorption line spectroscopy is more sensitive to changes in  $T_{\text{eff}}$  than broad-band photometry.

### 3.2 Chemical abundances

The Ca and Ni abundances were determined from features with little blending from other elements, mostly Fe lines. Several Ca spectral features are shown in Fig. 4a. In general, these features are well reproduced by the synthetic spectra, except for one feature ( $\sim 6450 \text{ Å}$ ), which was blended with an unidentified line in the Solar spectrum and which was not used in the chemical analysis. In Fig. 4b we show Si lines used in the abundance analysis. In Fig. 4c we show the region which contain the Al and Li doublets, and in Fig. 4d we show the O and Ni features.

The  $[\text{Fe}/\text{H}]$  ratio of  $0.48 \pm 0.04$  determined is surprisingly high,  $\sim 2$  times higher than that found in neutron star X-ray binaries (González Hernández et al. 2011). In Fig. 7 we show the element abundances of the secondary star in PSR J1023+0038 relative to Fe in comparison with the Galactic abundance trends (Adibekyan et al. 2012) as well as the element abundances of the secondary stars in X-ray binaries (González Hernández et al. 2011). We find that in general the abundances of the secondary star in PSR J1023+0038 are different to the elemental abundance of the secondary stars in other X-ray binaries and to stars in the Solar neighbourhood. The abundances ratios of Ca and Al, with respect to Fe in the secondary star of PSR J1023+0038 are higher than those in stars of similar Fe content (see Fig. 7) whereas, the Si abundance seems to be consistent with the Galactic trends of stars in the Solar neighbourhood. Ni and Al with respect to Fe are clearly enhanced compared to stars in the Solar neighbourhood.

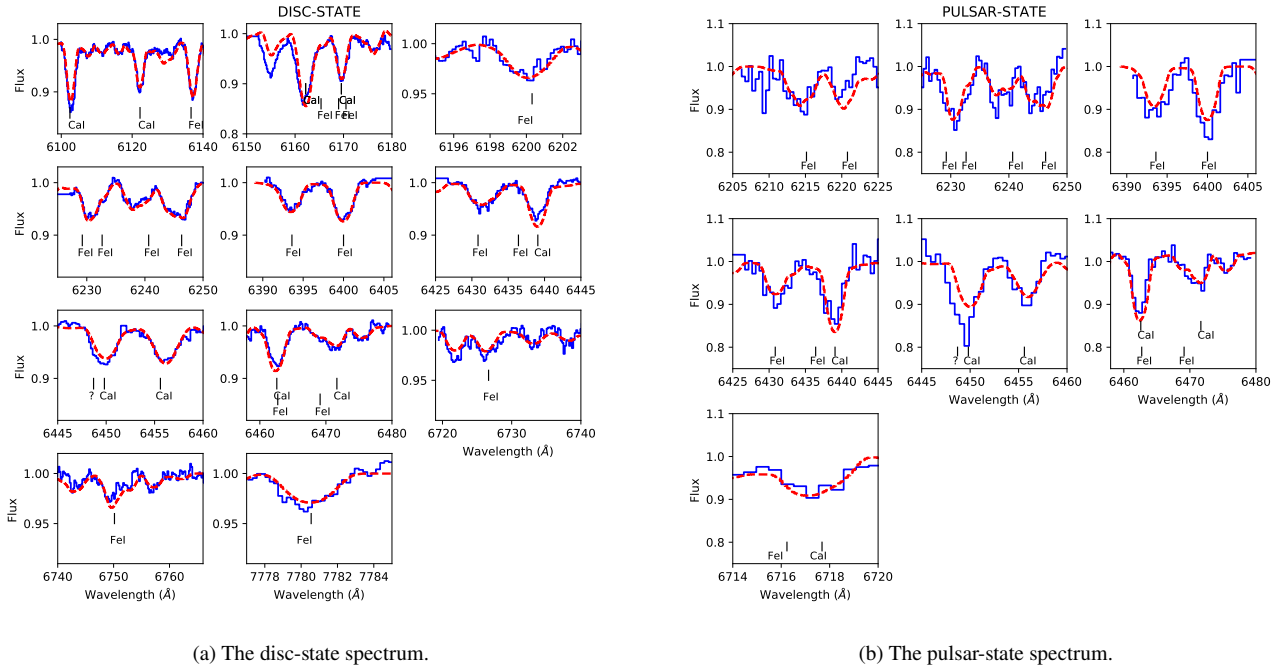


**Figure 3.** Sections showing the best-fit model (red dashed line) to the disc and pulsar-state spectrum (blue solid line) of the secondary star in PSR J1023+0038 used to determine the stellar parameters. The stellar parameters are given in Table 1 and Fig. 2

**Table 3.** LTE element abundances of black hole and neutron star X-ray binaries

Target	[O/H] <sup>a</sup>	[Al/H]	[Si/H]	[Ca/H]	[Fe/H]	[Ni/H]	A(Li) <sup>a,b</sup>	Ref. <sup>c</sup>
Black hole systems								
A0620–00		0.40 ± 0.12		0.10 ± 0.20	0.14 ± 0.20	0.27 ± 0.10	2.31 ± 0.21	1
XTE J1118+480		0.60 ± 0.20		0.15 ± 0.23	0.18 ± 0.17	0.30 ± 0.21	<1.8	4
Nova Sco 94	0.91 ± 0.09	0.05 ± 0.18	0.58 ± 0.08	−0.02 ± 0.14	−0.11 ± 0.09	0.00 ± 0.21	<2.16	5
V404 Cyg	0.60 ± 0.19	0.38 ± 0.09	0.36 ± 0.11	0.20 ± 0.16	0.23 ± 0.09	0.21 ± 0.19	2.70 ± 0.40	6
Neutron star systems								
Cen X–4		0.30 ± 0.17		0.21 ± 0.17	0.23 ± 0.10	0.35 ± 0.17	2.98 ± 0.29	2
Cyg X–2	0.07 ± 0.35	0.42 ± 0.05	0.52 ± 0.22	0.27 ± 0.05	0.27 ± 0.19	0.52 ± 0.05	<1.48	3
PSR J1023+0038	−0.64 ± 0.11	1.35 ± 0.09	0.50 ± 0.06	0.62 ± 0.06	0.48 ± 0.04	0.97 ± 0.23	3.66 ± 0.20	7

<sup>a</sup> Corrected for NLTE effects,

<sup>b</sup> Expressed as  $A(\text{Li}) = \log [N(\text{Li})/N(\text{H})] + 12$ .

<sup>c</sup> References: (1) González Hernández et al. (2004); (2) González Hernández et al. (2005); (3) Suárez-Andrés et al. (2015a); (4) González Hernández et al. (2008c); (5) González Hernández et al. (2008a); (6) González Hernández et al. (2011); Martin et al. (1992); (7) This work

### 3.2.1 Oxygen

The O abundance was derived from the O I near-infrared triplet O I 7771 Å in the disc-state spectrum (see Fig. 4) which is well reproduced by the synthetic spectra. The O I feature in the secondary star is under-enhanced compared with a template star having similar effective temperature (Solar abundance model). We obtain a best-fit LTE abundance ratio of  $[\text{O}/\text{Fe}]_{\text{LTE}} = -0.74 \pm 0.11$  dex, which corresponds to  $[\text{O}/\text{H}]_{\text{LTE}} = -0.26 \pm 0.12$  dex. The O I 7771 Å triplet suffers from significant non-LTE (NLTE) effects (Ecuivillon et al. 2006). For the stellar parameters and O abundance of the secondary star in PSR J1023+0038, the NLTE correction<sup>3</sup> is estimated to be

<sup>3</sup>  $\Delta_{\text{NLTE}} = A(X)_{\text{NLTE}} - A(X)_{\text{LTE}}$

$\sim -0.40$  dex. Applying this correction to the LTE O abundance leads to  $[\text{O}/\text{H}]_{\text{NLTE}} \sim -1.14$  dex, which implies that O is significantly depleted. In Table 2 we give the O abundance corrected for NLTE effects. The secondary star in PSR J1023+0038 has an anomalously low abundance ratio  $[\text{O}/\text{Fe}]_{\text{NLTE}} \sim -1.08$  dex which is clearly not consistent with the Galactic trend measured in stars in the Solar neighbourhood (see Fig. 7).

### 3.2.2 Lithium

The best-fit to the Li I 6708 Å feature gives an LTE abundance of  $A(\text{Li})_{\text{LTE}} = 4.09 \pm 0.20$  dex. Using 3D non-LTE model atmospheres

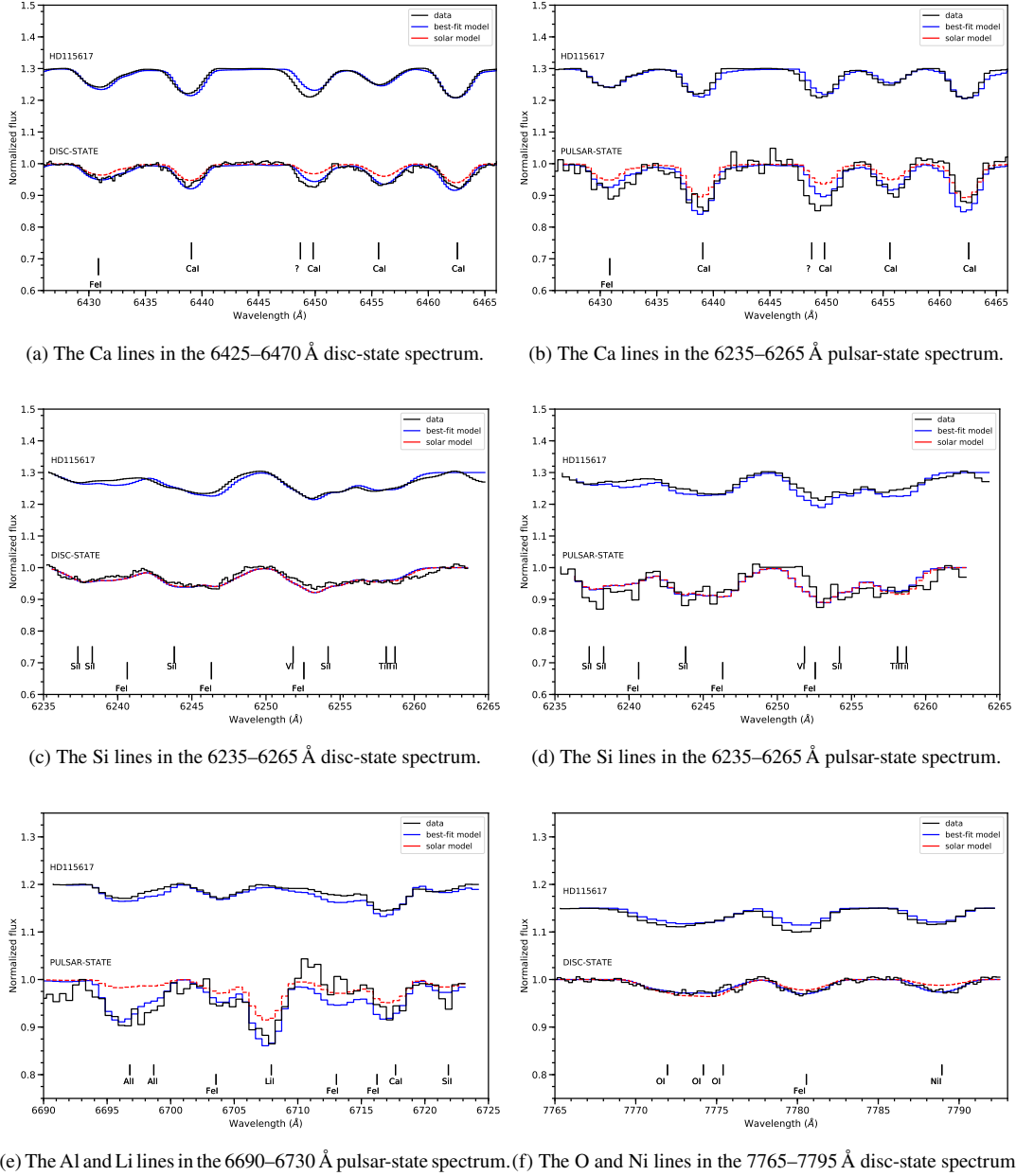


**Figure 4.** The best synthetic model fit synthetic model to the pulsar and disc-state spectrum of the secondary star in PSR J1023+0038. In each plot we also show fits to a G6 template star. The synthetic spectrum for Solarabundances (red dotted line) and best-fit abundances (blue solid line) are shown.

corrections (Wang et al. 2021), calculated using BREIDABLİK<sup>4</sup> we find  $\Delta\text{NLTE} \sim -0.43$  dex, which implies  $A(\text{Li})_{\text{NLTE}} = 3.66 \pm 0.20$  dex for the secondary star in PSR J1023+0038. For the template star spectrum HD 115617 we observe no Li and obtain results consistent with (Gonzalez et al. 2010). In Fig. 8 we compare the Li abundance of the secondary star in PSR J1023+0038 with the secondary stars in X-ray binaries and with stars in the Pleiades and Hyades cluster. The secondary star in PSR J1023+0038 has a Li abundance higher than late-type main sequence stars as well as X-ray binaries (see Section 4).

<sup>4</sup> <https://github.com/ellawang44/Breidablik>

#### 4 COMPARISON WITH YOUNG CLUSTERS AND X-RAY BINARIES

The secondary star in PSR J1023+0038 shows an unexpectedly high Li abundance, higher than the cosmic value seen in stars in the Galactic disk. Convective mixing is expected to deplete Li in the atmosphere of a G0 star during its pre-main sequence and main-sequence evolution. The mean Li abundance of stars in the 5700–6100 K temperature range decrease with age. This effect can be clearly seen in young open clusters such as the Pleiades cluster ( $\sim 110$  Myr; Dahm 2015) and the Hyades cluster ( $\sim 650$  Myr; Martín et al. 2018). In Fig. 8, we compare the Li abundance in PSR J1023+0038 with stars in the Pleiades and Hyades clusters. Clearly the Li content in the secondary star is too high compared

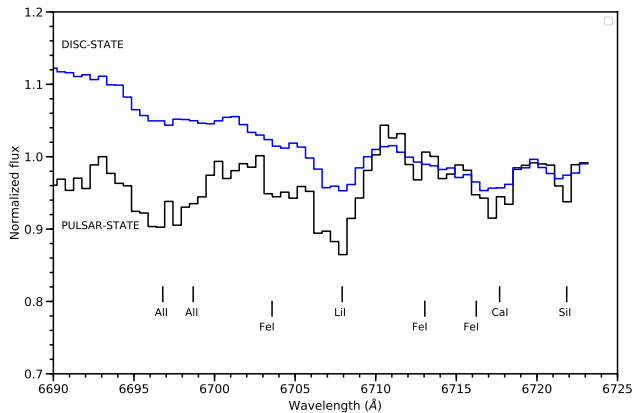


**Figure 5.** The pulsar- and disc-state (blue) spectra in the 6690–6730 Å spectral region showing the AlI 6696 Å and LiI 6708 Å doublets. Note the contamination of the disc-state spectrum from the broad HeII 6678 Å emission line arising from the accretion disc.

to stars with the same effective temperature, which indicates that in absence of a Li production mechanism, the secondary star in PSR J1023+0038 is much younger than the Pleiades cluster. [Francisini et al. \(2020\)](#) have studied the Li abundances of some young open clusters showing that the mean Li abundance of G0 stars decreases from  $A(\text{Li}) \sim 3.6\text{--}3.8$  dex in  $\gamma$ Velorum (10–20 Myr) to 3.2 dex in NGC2547 (35–45 Myr) down to about 3.0 dex in NGC 2516 (70–150 Myr) as in the Pleiades cluster ([Barrado et al. 2016](#)). [Lim et al. \(2016\)](#) measured Li abundance in a significant number of stars in the cluster NGC 2264 with  $T_{\text{eff}} = 4000\text{--}6500$  K, confirming that the initial Li abundance at ages 3–5 Myr is already around the cosmic value ( $A(\text{Li}) \sim 3.2 \pm 0.2$  dex). This demonstrates that the Li abundance of the secondary star in PSR J1023+0038 is anomalously high, irrespective of the age of the system. There are a few cases of unevolved stars (in this context, stars which have not reached the red giant branch; RGB) with extremely high Li content. One interesting example is a turn-off star #1657 in the metal-poor globular cluster NGC 6397, which shows  $A(\text{Li}) \sim 4.1$  dex ([Koch et al. 2011](#)), i.e. about 100 times higher Li content compared to the primordial Li abundance produced in the Big Bang. This result remains puzzling and unusual scenarios are involved in order to explain the strong Li enhancement, such as the capture of a substellar body, type-II supernovae, diffusion, contamination from an AGB/RGB companion, some of them excluded by the normal abundance of Be ([Pasquini et al. 2014](#)).

In general the abundances of heavy elements in the secondary star of PSR J1023+0038 are higher than the Solar value, and indeed higher than those of the most metal-rich stars of the Solar neighbourhood. In Fig. 7 we show the element abundances of the secondary star in PSR J1023+0038 relative to Fe in comparison with the Galactic abundance trends ([Adibekyan et al. 2012](#)) as well as the element abundances of secondary stars in other X-ray binaries ([González Hernández et al. 2011](#)). The abundances ratios of  $[\text{Ca}/\text{Fe}]$ ,  $[\text{Al}/\text{Fe}]$  and  $[\text{Ni}/\text{Fe}]$  are higher than those in stars of similar Fe content (see Fig. 7),  $[\text{O}/\text{Fe}]$  is surprisingly under-abundant and  $[\text{Si}/\text{Fe}]$  seems to be consistent with the Galactic trends of stars in the Solar neighbourhood.

The metallicity in the secondary star of PSR J1023+0038 ( $[\text{Fe}/\text{H}] \sim 0.48$ ) is much higher than the metallicity of other secondary stars in the neutron star X-ray binaries Cen X-4 and Cyg X-2 ([González Hernández et al. 2005](#); [Suárez-Andrés et al. 2015b](#)). In Cen X-4 and Cyg X-2, Ni is also over-abundant and in Cyg X-2 O ap-

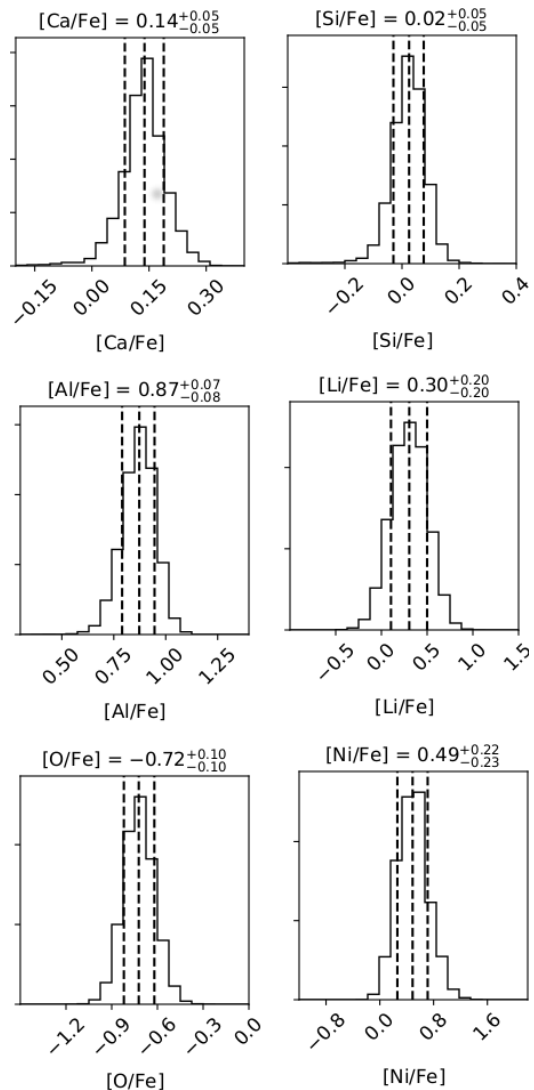


**Figure 6.** The results of the MCMC model parameter distributions resulting from synthetic fits to the observed spectrum of PSR J1023+0038 to determine the abundance of various elements. The projected 1-D parameter distributions with the mean and standard deviation are given in each plot.

pears to be under-abundant ([Suárez-Andrés et al. 2015b](#)). Indeed, the average metallicity of secondary stars in neutron star X-ray binaries ( $[\text{Fe}/\text{H}] \sim 0.24$ ) seems to be higher than in black hole X-ray binaries ( $[\text{Fe}/\text{H}] \sim 0.09$ ) ([González Hernández et al. 2011](#)), suggesting that a high amount of Fe is always ejected during SN explosions that forms the NS. The Li abundance is higher than field late-type main sequence stars as well as X-ray binaries (see Table 3).

## 5 CHEMICAL ANOMALIES DUE TO SUPERNOVA

It is generally believed that during the common envelope evolution of an interacting binary, a compact object (neutron star or black hole) is subsequently born after the explosion of the He star. Part of the ejected mass in the SN explosion may be captured by the secondary star, leading to abundance anomalies as for instance in the case of the black hole X-ray binary Nova Sco 1994 ([Israelian et al. 1999a](#); [González Hernández et al. 2008a](#)). The chemical abundances of the secondary stars in X-ray binaries show over-abundance of several  $\alpha$ -elements



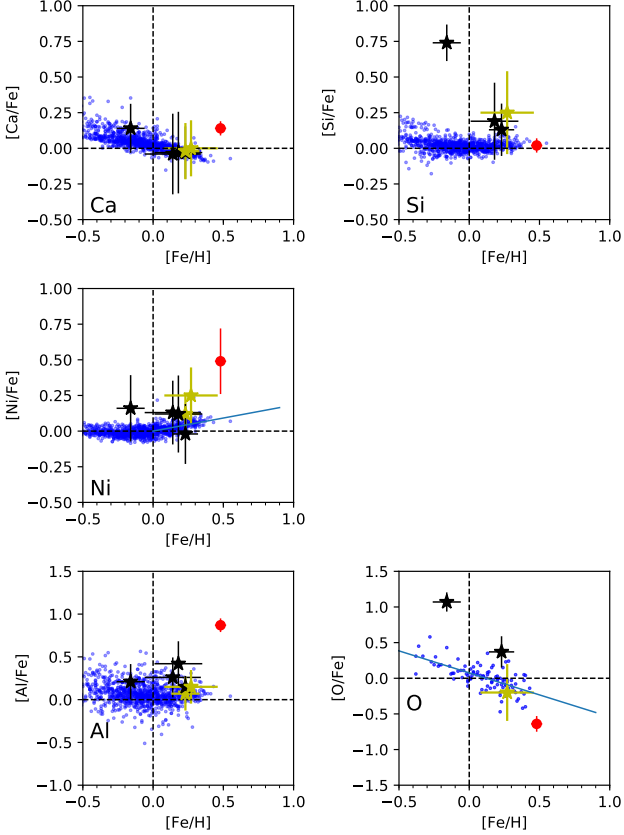


**Figure 7.** Abundance ratios of the secondary star in black hole (black stars) and neutron star (yellow stars) X-ray binaries (see Table 3) in comparison with the abundances of solar-type stars in the Solar neighbourhood (blue circles). The red circles show the abundance ratio in PSR J1023+0038. Galactic trends are taken from Adibekyan et al. (2012) and Ecuivillon et al. (2006). [O/Fe] has been corrected for NLTE effects.

(such as O, S, Si, Ca). This has been interpreted as pollution by matter ejected during the SN/HN (see González Hernández et al. 2011, and references within). In the following we consider this scenario for PSR J1023+0038.

### 5.1 Spherical Explosion

Following the arguments outlined in González Hernández et al. (2011), we can estimate the maximum ejected mass in the SN explosion that could be captured by the secondary star. Shahbaz et al. (2019) estimate the current neutron star and secondary star mass to be  $M_{\text{NS},f} \sim 1.76 M_{\odot}$  and  $M_{2,f} \sim 0.24 M_{\odot}$ , respectively. Furthermore, the neutron star is expected to have accreted material during the binary evolution, and so we adopt a canonical neutron star initial mass of  $M_{\text{NS},i} \sim 1.4 M_{\odot}$ .

The binary system will survive a spherical SN explosion if the following condition for the ejected mass is satisfied,  $\Delta M = M_{\text{He}} - M_{\text{NS},i} \leq (M_{\text{He}} + M_{2,i})/2$ , where  $M_{\text{He}}$  is the helium core mass of the progenitor star before the SN. For the sake of the argument, if we adopt  $M_{\text{He}} \sim 4 M_{\odot}$ , an ejected mass of  $\sim 2.6 M_{\odot}$  implies an initial mass for the secondary star of  $M_{2,i} \geq 1.2 M_{\odot}$ . Therefore, in what follows we assume a secondary star mass of  $M_{2,i} \sim 1.3 M_{\odot}$ . Furthermore, using the expressions given by Portegies Zwart et al. (1997) one can infer mass of the progenitor star,  $M_{1,i} \sim 16.7 M_{\odot}$ ,

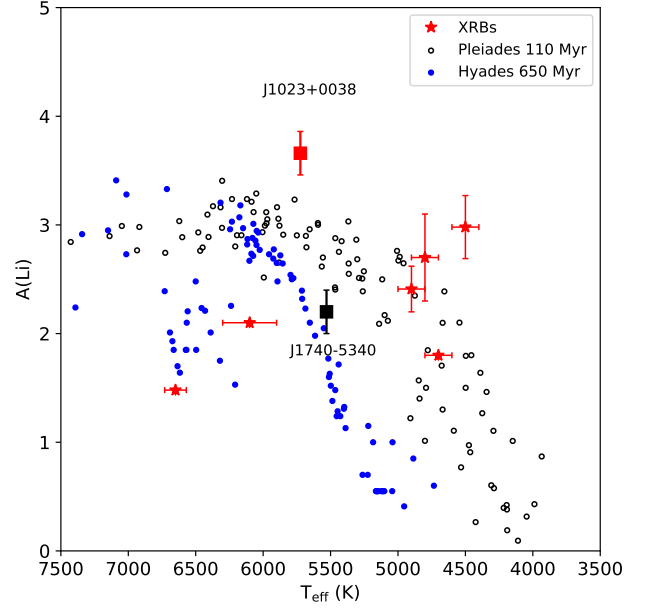


**Figure 8.** Li abundance of the secondary star in PSR J1023+0038 (filled blue circle) in comparison with the secondary stars in X-ray binaries (red filled stars) and stars in the young clusters, Pleiades (Barrado et al. 2016) and Hyades (Cummings et al. 2017).

and the radius of the helium core  $R_{\text{He}} \sim 0.9 R_{\odot}$ . The current orbital period of PSR J1023+0038 measured from pulsar timing (Archibald et al. 2013) is  $P_{\text{orb}} \sim 0.198$  d ( $\sim 4.754$  hr). This, together with the mass of the neutron star, the secondary star and Kepler’s third law, gives a current orbital separation of  $a_{c,f} \sim 1.79 R_{\odot}$ . However, during the binary evolution of the system the secondary must have experienced mass and angular momentum losses leading to a decrease in the orbital separation to its present configuration. We therefore assume the post-SN orbital separation after tidal circularisation of the orbit to be  $a_{c,i} \sim 3 R_{\odot}$ .

Assuming a pre-SN circular orbit and an instantaneous, spherically symmetric ejection one can estimate the orbital separation just before the SN,  $a_0$ , and after tidal circularisation,  $a_{c,i}$ , of the post-SN eccentric orbit using the relation given by van den Heuvel & Habets (1984):  $a_0 = a_{c,i} \mu_f$ , where  $\mu_f = (M_{\text{NS}} + M_{2,i}) / (M_{\text{He}} + M_{2,i})$ . We adopt a secondary initial mass of  $M_{2,i} \sim 1.3 M_{\odot}$ , which implies a pre-SN orbital separation of  $a_0 \sim 1.5 R_{\odot}$ , which is larger than the estimated radius of the He core. The secondary star at the time of the SN explosion (at about 7 Myr) would still be in the pre-main sequence evolutionary stage and so will have a radius of  $R_{2,i} \sim 1.5 R_{\odot}$ , estimated from the pre-main sequence PARSEC<sup>5</sup> isochrone (see e.g. Bressan et al. 2012). Part of the matter ejected in the SN explosion is expected to be captured by the secondary star, thus polluting its atmosphere with SN nucleosynthesis products. The fraction of the matter ejected in the direction of the secondary star that is finally captured can be estimated as  $m_{\text{cap}} = \Delta M (\pi R_{2,i} / 4\pi a_0^2) f_{\text{cap}}$ , where  $f_{\text{cap}}$  is the fraction of mass ejected within the solid angle subtended by the secondary star, that is eventually captured. We assume that the captured mass,  $m_{\text{cap}}$  (heavier matter compared to the stellar material of the secondary star) is completely mixed with the rest of the companion star.

<sup>5</sup> PARSEC isochrones are available at <http://stev.oapd.inaf.it/cgi-bin/cmd>

**Table 4.** Expected abundances from supernova explosion models in PSR J1023+0038.

Element	A(X) <sub>⊙</sub> <sup>d</sup>	[X/H]	δ[X/H]	Spherical <sup>a</sup>			Aspherical <sup>b</sup>			Aspherical* <sup>c</sup>		
				$m_{\text{cut}} [M_{\odot}]$			$m_{\text{cut}} [M_{\odot}]$			$m_{\text{cut}} [M_{\odot}]$		
				1.31	1.40	1.49	1.28	1.36	1.45	1.49	1.55	1.77
O	8.74	-0.64	0.11	0.56	0.54	0.52	0.77	0.75	0.68	0.50	0.49	0.46
Al	6.47	1.35	0.09	0.79	0.76	0.74	1.03	1.00	0.95	0.70	0.69	0.66
Si	7.55	0.50	0.06	0.83	0.80	0.73	1.08	0.83	0.67	0.75	0.74	0.53
Ca	6.36	0.62	0.06	0.60	0.56	0.34	0.82	0.33	0.29	0.63	0.56	0.07
Fe	7.50	0.48	0.04	0.81	0.57	0.04	0.52	0.32	0.21	0.63	0.37	0.00
Ni	6.25	0.97	0.23	1.24	0.56	0.02	0.43	0.30	0.12	0.78	0.31	0.00
$Q^e$				0.30	0.25	1.19	0.65	0.64	0.90	0.11	0.48	1.44

<sup>a</sup> Spherically symmetric explosion (Spherical).

<sup>b</sup> Non-spherically symmetric explosion (Aspherical).

<sup>c</sup> Non-spherically symmetric explosion with complete lateral mixing (Aspherical\*).

<sup>d</sup> Solar abundances are taken from [Grevesse et al. \(1996\)](#) and [Ecuivillon et al. \(2006\)](#) for O.

<sup>e</sup> O and Al have not been included.

We compute the expected abundances in the secondary star after the pollution from a SN explosion as in ([González Hernández et al. 2004](#); [González Hernández et al. 2008a](#)). We firstly examine a spherically symmetric core-collapse SN of a 4  $M_{\odot}$  He core ([Maeda et al. 2002](#); [González Hernández et al. 2005](#)) with a explosion energy of  $E_K = 10^{51}$  erg (see Table 4). We adopt a companion star with a mass of  $M_{2,i} \sim 1.3 M_{\odot}$  with initial Solar abundances and an orbital separation of  $a_{c,i} = 3 R_{\odot}$ . We find that we require a capture efficiency of  $f_{\text{cap}} = 0.10\text{--}0.30$  in order to reproduce the observed Fe abundance increase from the initial Solar value, which depends on the mass cut,  $m_{\text{cut}}$ . The mass cut can be understood as the initial mass of the compact object. For the case of neutron stars, we assume there is no fallback material, so the mass cut reflects the initial mass of the neutron star, and the ejected mass is just the difference between the mass of the He core and the mass cut. In Fig. 9a we compare the observed abundances in PSR J1023+0038 with expected abundances from three different spherical models. We assume a capture efficiency of  $f_{\text{cap}} = 0.30$  and different mass cut values (see Table 4). In order to quantify the comparison between the observed and model abundances we determine the variance,  $Q$ .

The mass captured in these three models are in the range 0.16–0.20  $M_{\odot}$ . Fe-peak elements such as Fe and Ni are formed in the inner layers of the SN explosion, and therefore the lower the mass cut, the more Fe and Ni products in the ejecta that can eventually enrich the atmosphere of the secondary star (see Fig. 9).  $\alpha$ -elements such as Si and Ca are less sensitive to changes in this mass cut range 1.31–1.49  $M_{\odot}$ . Si appears to be about 0.4 dex more abundant for all mass cuts, while Ca seems to be consistent for mass cuts below 1.4  $M_{\odot}$  in these models with respect to the observed abundances. O and Al remain mostly independent of the adopted mass cut as these elements form in the outer layers of the SN explosion and, in all models, O is too high and Al is too low with respect to the observed abundances in PSR J1023+0038.

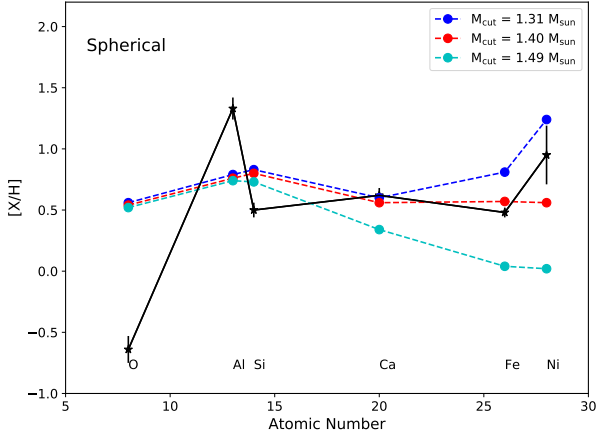
## 5.2 Non-spherical (aspherical) explosion

The neutron star in PSR J1023+0038 could have been formed in a non-spherically symmetric explosion. Chemical abundance studies in two other neutron star X-ray binaries, Cen X-4 ([González Hernández et al. 2005](#)) and Cyg X-2 ([Suárez-Andrés et al. 2015a](#)), arrive at different conclusions. The case of Cen X-4 favors a spherical explosion, whereas the observed abundances in Cyg X-2 seems to be better

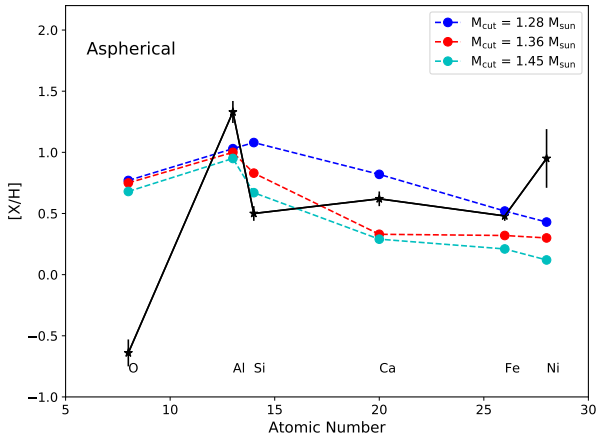
reproduced using aspherical explosion models. The general scenario extracted from the analysis of the spectra of SN is that neutron stars can form via normal less-aspherical SN explosions ( $E_K = 10^{51}$  erg) from relatively low mass primary stars ( $M_1 \leq 20 M_{\odot}$ ), as suggested by [Umeda & Nomoto \(2003\)](#). A more massive primary star ( $M_1 \sim 40 M_{\odot}$ ) can explode as an aspherical hypernova (HN) with a kinetic energy of  $E_K = (10 - 30) \times 10^{51}$  erg, leaving behind a black hole, as proposed to explain the enhanced observed abundances of some  $\alpha$ -elements in the black hole X-ray binary Nova Sco 1994 (see e.g. [Israeli et al. 1999b](#); [Brown et al. 2000](#); [Podsiadlowski et al. 2002](#)). However, [González Hernández et al. \(2008a\)](#) performed a detailed chemical analysis of Nova Sco 1994, including additional elements such as Al and Ca, which are formed in the outer and inner layers of the explosion respectively. They concluded that a spherically symmetric and more energetic HN model is favored in this system.

Large systemic velocities are observed in neutron star X-ray binaries,  $\gamma \sim +190 \text{ km s}^{-1}$  and  $\gamma \sim -210 \text{ km s}^{-1}$  for the Cen X-4 ([Casares et al. 2007](#)) and Cyg X-2 ([Casares et al. 2010](#)), respectively. The large systemic velocities can be interpreted as a kick in the formation of the compact object due to an asymmetric SN/HN explosion. In contrast PSR J1023+0038 has a small systemic velocity  $\gamma \sim 5.2 \text{ km s}^{-1}$  ([Shahbaz et al. 2019](#)). Using the parallax and proper motions from Gaia eDR3 ([Gaia Collaboration et al. 2020](#)) with the observed systemic radial velocity we can determine the 3D velocity of the system (i.e. the velocity relative to expected motion in the Galaxy). We use the method outlined in [Reid et al. \(2009\)](#) to transform the observed parameters into heliocentric space velocities, and then remove Solar motion as well as Galactic rotation and find a peculiar velocity of  $131 \text{ km s}^{-1}$ .

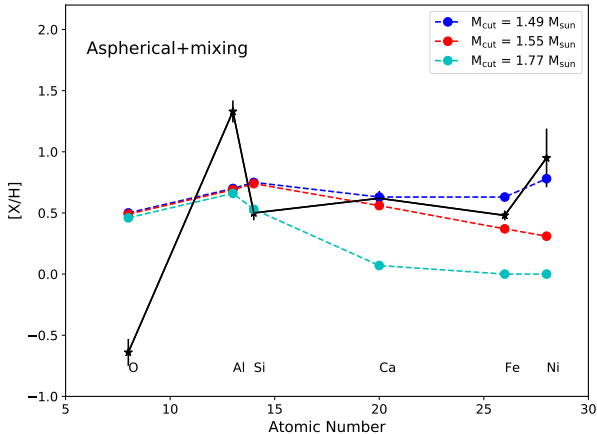
We can compare the peculiar velocity to the expected impulse velocity due to symmetric mass ejection during a SN explosion. Assuming a 4.0  $M_{\odot}$  He core and a secondary star of 1.3  $M_{\odot}$  which produces a bound system with a 1.4  $M_{\odot}$  neutron star and a post-SN orbital separation of  $a_{c,i} \sim 3 R_{\odot}$ , provides an impulse (Blaauw-Boersma kick; [Blaauw 1961](#); [Boersma 1961](#)) velocity of  $v_{\text{sys}} \sim 192 \text{ km s}^{-1}$  ([Nelemans et al. 1999](#); [Brown et al. 2001](#)). Assuming a He core mass of 3.0  $M_{\odot}$  and a secondary mass of 1.3  $M_{\odot}$  produces an impulse velocity of  $v_{\text{sys}} \sim 118 \text{ km s}^{-1}$ . These observed velocities do not appear to support a significant mass ejection in the SN explosion and suggest that an additional natal kick from an asymmetric SN may not be required. However, aspherical explosions can produce



(a) Spherically symmetric core-collapsed SN explosion.



(b) Aspherical symmetric core-collapsed SN explosion.



(c) Aspherical symmetric core-collapsed SN explosion with lateral mixing

**Figure 9.** Expected abundances in the secondary atmosphere due to the pollution caused by (a) a spherically symmetric core-collapsed SN explosion model (top panel), (b) a non-spherically symmetric (or aspherical) SN explosion model (middle panel) and (c) an aspherical SN explosion (bottom panel) with complete lateral mixing (see text and also Table 4). The models are computed for different mass-cuts,  $M_{\text{cut}}$ , assuming a progenitor mass of  $M_{\text{He}} = 4.0 M_{\odot}$ , a secondary star initial mass of  $M_{2,i} = 1.3 M_{\odot}$ , and fixed values for  $f_{\text{cap}} = 0.30, 0.50$  and  $0.40$ . In all cases an orbital separation of  $a_{c,i} = 3 R_{\odot}$  and a kinetic energy of  $E_K = 1 \times 10^{51}$  erg is assumed. The black stars show our measurements for PSR J1023+0038.

chemical abundance anomalies in the ejecta that cannot be produced in spherically symmetric explosion models. Therefore, in the following we also examine the possible contamination of the atmosphere of the secondary star from a non-spherically symmetric (aspherical) SN.

A non-spherical SN explosion can produce chemical inhomogeneities in the ejecta which are dependent on direction. If the collimated jet of an aspherical SN explosion is perpendicular to the binary orbital plane, elements such as Ti, Fe, and Ni are ejected mainly in the jet direction, while O, Mg, Al, Si, and S are preferentially ejected near the equatorial plane of the helium star (Maeda et al. 2002) and thus expected to be enhanced in the atmosphere of the secondary star.

In Fig. 9b we show the expected abundances in the secondary’s atmospheres from an aspherical explosion of a  $4.0 M_{\odot}$  He core. Fe and Ni are preferentially ejected perpendicular in the orbital plane only with a mass cut below  $1.3 M_{\odot}$  and with a capture efficiency of  $f_{\text{cap}} = 0.50$ , which implies a significant fraction of mass ( $0.30$ – $0.36 M_{\odot}$ ) is captured by the secondary. Even with these parameters the amount of Ni in the SN model is about  $0.5$  dex lower than the observed abundance. Si, Ca, Fe and Ni are highly dependent on mass cut in the range  $1.28$ – $1.45 M_{\odot}$ . In particular Ca is only highly enhanced for the lowest mass cut at  $1.28 M_{\odot}$ . O and Al are mainly ejected in the equatorial plane, and thus only depend on the capture efficiency, and they behave similar to the spherical model (Fig. 9a) with respect to the observed abundances.

Finally, in Fig. 9c, we also consider an aspherical explosion model with the extreme assumption of complete lateral mixing (see Maeda et al. 2002; Podsiadlowski et al. 2002, for further details), where the ejected matter is completely mixed with each velocity bin (González Hernández et al. 2008a). This model requires  $f_{\text{cap}} = 0.40$  with a captured mass of  $0.19$ – $0.22 M_{\odot}$ . As in the case of the spherical SN explosion, the expected abundances of Si, Ca, Fe and Ni show a dependence with mass cut in the range  $1.49$ – $1.67 M_{\odot}$ . Qualitatively, the spherical model with  $m_{\text{cut}} = 1.31 M_{\odot}$  and the aspherical model with  $m_{\text{cut}} = 1.49 M_{\odot}$  agree better with the observations. However, as with all the other models, we cannot reconcile the O and Al observed abundances.

Nomoto et al. (2010) argue that more energetic HNe are produced by more massive progenitors of compact objects (likely black holes) which may be more asymmetric than normal SNe that show different levels of kinetic energies (Maeda et al. 2006). We have not been able to favor the spherical explosion over the aspherical in the case of PSR J1023+0038. The high element abundances derived in PSR J1023+0038, in particular, the high content in Fe-peak elements support the formation of a neutron star in a SN. This new Fe measurement in this MSP contributes to the detection of Fe in other neutron star X-ray binaries where also a high Fe abundance has been reported and supports the idea that the formation of neutron star in normal less massive SNe ejects a significant fraction of  $^{56}\text{Ni}$ . However, Nomoto et al. (2010) also argue that more energetic HNe that may led to the formation of black holes are expected to eject larger quantities of  $^{56}\text{Ni}$  than less massive progenitors of neutron stars that explode with lower kinetic energies and presumably smaller amounts of  $^{56}\text{Ni}$ .

### 5.2.1 Other chemical elements

In the following sections we discuss also the evolution of CNO and Li in the atmosphere of the secondary star. C and N are produced in the outer layers of both spherical and aspherical SN explosions. The expected abundances of C and N follow the same behaviour as O in the models with lower levels of production at  $[C/H] = 0.40$ – $0.60$  and

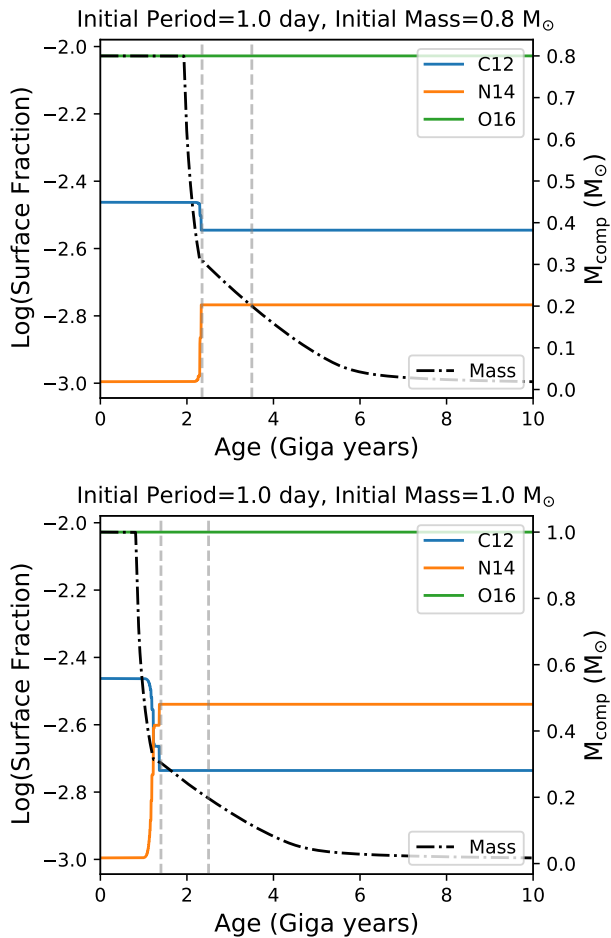


**Figure 10.** The results of MESA simulations using the angular momentum loss of [Chen et al. \(2013\)](#). The initial period of the binary is 1 d, while the initial masses of the secondary star are  $0.8 M_{\odot}$  (top plot) and  $1.0 M_{\odot}$  (bottom plot). The  $^{12}\text{C}$  (blue),  $^{14}\text{N}$  (orange) and  $^{16}\text{O}$  (green) elemental surface fraction are shown as time. The secondary star’s mass (black dot-dashed line) remains constants until it comes into contact with the Roche lobe and then decreases very rapidly until it reaches  $\sim 0.3 M_{\odot}$ , in which case magnetic braking turns off, and mass transfer slows down. The C and N surface composition after  $t \sim 2.2$  Gyr on the left plot ( $\sim 1.32$  Gyr on the right plot) remains constant because magnetic braking has turned off, even though the companion star continues to loose mass.

$[\text{N}/\text{H}] = 0.10\text{--}0.15$ . Unfortunately, we do not have C and N features to measure abundances in PSR J1023+0038 in the spectral range available in this work. Li is not present in these SN explosion models. The mass fraction of Li in the ejecta of the models evaluated in this work is negligible. The production of Li in core-collapse SN has been studied by [Woosley & Weaver \(1995\)](#), suggesting  $^7\text{Li}$  production as a consequence of a sufficiently high neutrino irradiation in the SN model. However, [Prantzos \(2012\)](#) argues against a significant role of core-collapse SN in the production of Li in the Galaxy.

## 6 CHEMICAL ABUNDANCE ANOMALIES DUE TO CNO EVOLUTION

After the SN explosion, the subsequent evolution is driven by strong mass-loss, most of which is accreted by the neutron star. Over the

last number of years, the consensus that has developed in the community is that the efficiency of angular momentum loss from the binary, whether driven by magnetic braking or through irradiation feedback, is a key factor in determining whether a binary evolves into a black widow, a redback, or a pulsar and white dwarf binary ([Chen et al. 2013](#); [Jia & Li 2015](#); [Van et al. 2019](#); [Van & Ivanova 2019](#)). This efficiency is inherently linked to the evolutionary status of the companion. As a consequence of mass-loss and nuclear evolution, a convective envelope develops and penetrates to deep layers of the star, which are then mixed, changing the star’s surface chemical composition. If the star’s surface is exposed to material that has undergone partial CNO burning, its composition should show the signature of CNO processing where C depletion (and if significant CNO burning has occurred, also O depletion) and N enhancement are expected ([Clayton 1983](#)). As such, the C/O ratio and C/N ratio of a given binary can be used to infer the evolutionary status of the companion star prior to the start of mass transfer ([Nelemans et al. 2010](#)). This has been successfully applied to differentiate the formation channels for the hydrogen deficient companions of white dwarfs in short orbital period ( $<70$  min) systems (e.g. [Kennedy et al. 2015](#); [Kupfer et al. 2016](#)), where the ratio of N and O relative to C has revealed whether the companion is a low mass helium star or slightly evolved, post-main sequence star. It has also been seen in an X-ray binary system ([Ergma & Sarna 2001](#)) that there is a decrease in the surface  $^{12}\text{C}/^{13}\text{C}$  ratio, with a corresponding increase in  $^{14}\text{N}$  and decrease in  $^{15}\text{N}$ , so the  $^{14}\text{N}/^{15}\text{N}$  ratio increases with respect to the initial value. The  $^{16}\text{O}$  abundance remains unaltered, while that of  $^{17}\text{O}$  increases.

The evolutionary models proposed for redbacks and black widows are also capable of making predictions for the chemical abundances at the stellar surface of the companion. While a full, detailed study of the effects of the initial binary parameters and the strength of the angular momentum loss on the chemical composition of redback companions is beyond the scope of the current work, we have reproduced selected models discussed in [Chen et al. \(2013\)](#) and in [Van & Ivanova \(2019\)](#) using Modules for Experiments in Stellar Astrophysics (MESA version 15140; [Paxton et al. 2013](#); [Paxton et al. 2019](#)). The C, N and O abundance at the surface appears to be tightly controlled by a combination of the rate of angular momentum loss and the initial conditions of the binary. For inefficient angular momentum loss and where the donor star evolves significantly before the onset of mass transfer, we produce companions which resemble the hydrogen deficient companions of white dwarfs previously mentioned, with no detectable H or C at their surface, very little O, and significant N. This is at odds with the spectrum of the companion of PSR J1023+0038, which still shows strong hydrogen features. For efficient angular momentum loss, we produce companions with overabundant O, slightly overabundant N, no C, and typical amounts of H.

[Fig. 10](#) shows the results of two intermediate cases, where we have used the angular momentum loss of [Chen et al. \(2013\)](#). In both, the initial period of the binary is 1 d, while the initial masses of the donor star are  $0.8 M_{\odot}$  and  $1.0 M_{\odot}$ , respectively. As mass-loss from the secondary star commences, the  $^{14}\text{N}/^{12}\text{C}$  ratio quickly changes, reaching a new equilibrium value once the star has become fully convective and angular momentum loss due to magnetic braking switches off. This shows that we do expect modest  $^{14}\text{N}$  enhancement in binaries which produce companions similar to the one in PSR J1023+0038, while  $^{16}\text{O}$  is untouched in these models. A more robust study on the relationship between the chemical composition of the secondary stars in spider binaries and their binary evolution is required to better understand the anomalous abundances seen in PSR J1023+0038.

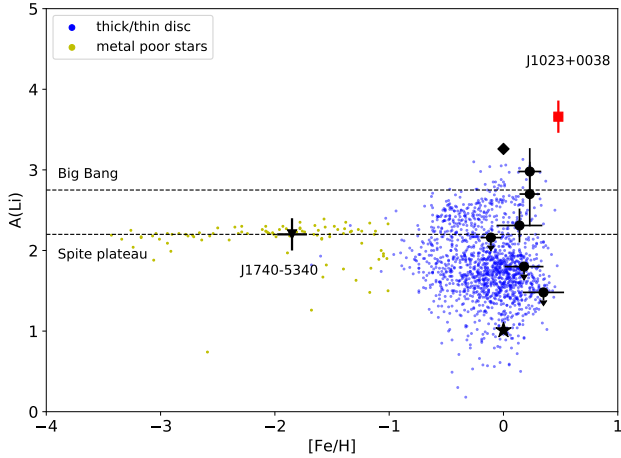


**Figure 11.** Li abundances as a function of  $[\text{Fe}/\text{H}]$ . The yellow and blue dots show the Li abundance of metal poor stars (Meléndez et al. 2010) and the thick/thin disc (Fu et al. 2018), respectively. The primordial  ${}^7\text{Li}$  abundance value  $A(\text{Li}) = 2.75$  dex determined from Standard Big Bang Nucleosynthesis models (Pitrou et al. 2018) and the ‘Spite plateau’ at  $A(\text{Li}) \sim 2.2$  dex determined from metal-poor Population II halo dwarf stars (Spite & Spite 1982) are shown as dashed lines. The value we obtain for PSR J1023+0038 (red square) is also shown along with the value obtained for the black widow pulsar PSR J1740–5340 (black filled triangle; Sabbi et al. 2003) and the values obtained in X-ray binaries (black filled circle; see Table 3). We show the Solar value (black star) of  $A(\text{Li}) = 1.01$  dex (Anders & Grevesse 1989), meteoritic value (black diamond) of  $A(\text{Li}) = 3.26$  dex (Asplund et al. 2009).

The only MSP where a spectroscopic chemical abundance analysis exists is for PSR J1740–5340, which lies in the globular cluster NGC 6397 (D’Amico et al. 2001). PSR J1740–5340 is a redback MSP which has a  $\sim 0.3 M_{\odot}$  secondary star in a 32.5 hr binary orbit (Ferraro et al. 2001; Orosz & van Kerkwijk 2003). There is a complete absence of C and the enhanced N in the atmosphere indicates a composition resulting from the hydrogen-burning CNO cycle. Ergma & Sarna (2003) computed evolutionary models for PSR J1740–5340 to predict the surface chemical composition as a function of the secondary mass. For the case of an evolved star which has lost mass, O would have a normal abundance, whereas N would be overabundant and C under-abundant, suggesting that the secondary star in PSR J1740–5340 is a low-mass ( $0.3 M_{\odot}$ ) remnant star of a deeply peeled star  $0.8 M_{\odot}$  progenitor (Mucciarelli et al. 2013).

In PSR J1023+0038 we find  $[\text{O}/\text{Fe}]$  is under-abundant compared with the Galactic trends of stars in the Solar neighbourhood. Unfortunately, due to our spectral range coverage we cannot measure the C or N abundances in PSR J1023+0038. This means that we cannot fully test CNO processing models. However, given that one expects normal O abundance, in contrast to what we observe suggests that underabundant O in PSR J1023+0038 is not due to chemical anomalies associated with the CNO cycle.

## 7 LITHIUM AROUND COMPACT OBJECTS

Li is a complex element and can be created in a number of ways such as Big Bang nucleosynthesis, in the cool bottom burning process during the asymptotic giant branch (AGB) phase, or via spallation of CNO nuclei. On the other hand, it is easily destroyed in the stellar interiors.

The primordial Li abundance is preserved in stars that are old

and comparatively cool. Since nuclear-fusion reactions take place in the star’s inner hot regions, the composition of the outermost layers of old stars indicates the initial chemical content at the time of the star’s formation and so abundances should be close to the primordial values. The observed ‘lithium plateau’ in the  ${}^7\text{Li}$  abundance of metal-poor Population II halo dwarf stars at  $A(\text{Li}) \sim 2.2$  dex is well-established (Spite & Spite 1982) and is often interpreted as due to a depletion in  ${}^7\text{Li}$  from the primordial cosmological value of  $A(\text{Li}) = 2.75$  dex predicted by Standard Big Bang Nucleosynthesis models (Pitrou et al. 2018) in the course of stellar evolution (e.g. Charbonnel & Primas 2005; Cyburt et al. 2008). This discrepancy is generally denominated as the ‘cosmological lithium’ problem. Many studies have been devoted to solve this problem (see Mathews et al. 2020, for a review).

As stars evolve Li is pulled to hot deep layers and gradually destroyed via proton capture ( $p, \alpha$ ) reactions in the hotter stellar regions with a temperature of a few  $10^6$  K (Pinsonneault 1997). Li at the surface layers is also expected to be depleted via various processes, such as atomic diffusion (Michaud 1986), rotational mixing (Pinsonneault et al. 1992) or convection overshooting (Xiong & Deng 2009) which can lead to a significant reduction in the Li abundance in the star’s atmosphere as it evolves.

The Li abundance in young Population I stars is equal to the meteoritic value of  $A(\text{Li}) = 3.26$  dex (Asplund et al. 2009) which is an indirect indication of the Li abundance in the interstellar gas-dust medium from which these stars were formed. This is an order of magnitude greater than the Li abundance found in old stars in the halo (the ‘lithium plateau’) which indicates that the Galaxy has undergone a history of Li enrichment since the Big Bang. To reach the high  ${}^7\text{Li}$  values found in meteorites, which is generally accepted to be the typical initial Li abundance of Population I stars, requires Galactic Li enrichment. Mechanisms of Li enhancement in the Galaxy include cosmic-ray spallation interactions in the interstellar medium (Reeves et al. 1970), core-collapse SN, (Woolsey et al. 1990), novae (Hernanz et al. 1996) or in evolved low-mass stars (see Prantzos et al. 2017; Matteucci et al. 2020, and references within).

Li is easily ionized (its ionization potential is 5.39 eV), so Li I line is only observed in relatively cold stars with effective temperatures less than 8500 K corresponding to stars with a spectral type ranging from late A to M. The analysis of the strong Li I resonance line at  $6707.8 \text{ \AA}$  provides data for the  ${}^7\text{Li}$  abundance in these stars. In Fig. 11 we show the  ${}^7\text{Li}$  abundance of metal-poor dwarf stars and the primordial  ${}^7\text{Li}$  abundance value, as well as the  ${}^7\text{Li}$  abundance we observe in PSR J1023+0038.

The observed Li abundance in neutron star and black hole quiescent X-ray transient binaries is relatively high, but not in excess of the meteoritic value (see Table 3). This is surprising as Li is destroyed/depleted in stellar interiors. However, Li can also be preserved. Heating of the secondary star’s surface by high energy radiation produced near the compact object may stabilize the outer layers to convection, so that the light elements in these layers are never driven to the depths at which they are destroyed (Eichler & Nath 1996). Rotation might also reduce Li suppression mechanisms, in that the tidally locked rotation of the secondary star naturally leads to slower Li destruction rates leading to Li abundances closer to the standard value at formation for Population I stars (Maccarone et al. 2005). To some extent this is supported by the measurement of the  ${}^6\text{Li}/{}^7\text{Li}$  isotopic ratio in Cen X–4 (Casares et al. 2007). Clearly, the definite proof of Li production would be to determine a Li abundance higher than the cosmic value.

In Fig. 11 we show the  ${}^7\text{Li}$  primordial abundance and the abundance in metal-poor galactic Halo and thin/thick disc stars. We also

show the  ${}^7\text{Li}$  abundance measured in PSR J1023+0038 with  $A(\text{Li}) = 3.66 \pm 0.20$  dex which is greater than the meteoritic value and what is observed in young Population I stars at the  $2\sigma$  level, providing evidence for Li enhancement in the atmosphere of the secondary star. It should be noted that enhanced Li is also observed in the red-back pulsar PSR J1740–5340 containing a subgiant secondary star with  $A(\text{Li}) = 2.2 \pm 0.2$  dex, which is higher than what is expected for evolved subgiant stars  $A(\text{Li}) \sim 1.5$  dex (see Sabbi et al. 2003, and references within). As suggested by the authors, the most plausible explanation is fresh Li production due to nuclear reactions occurring on the stellar surface induced by the cosmic-rays produced by the pulsar. In the following sections we outline plausible explanations for the Li enhancement in PSR J1023+0038.

## 8 LI ENHANCEMENT

### 8.1 Spallation via neutrons

As outlined in various papers, the conditions around compact objects are ideal for Li production via the acceleration of relativistic particles and spallation in the inner accretion flow or in the stellar atmosphere (Martin et al. 1995; Yi & Narayan 1997; Guessoum & Kazanas 1999; Fujimoto et al. 2009). The quiescent black hole and neutron star X-ray binaries have hot advection-dominated accretion flows (ADAFs; Narayan & Yi 1995; Narayan et al. 1996; Menou et al. 1999). The ion temperature around black holes and neutron stars is very similar and can be predicted by the basic assumptions set in the ADAF in which the ions are first heated by the viscous processes, and then a fraction of this heat energy which is stored in the ions is transferred to the electrons via Coulomb collision. Given the low gas density in the ADAF, the Coulomb collision is not efficient and so the amount of heat energy transferred to the electrons is small. Consequently, the ions are kept at a relatively higher temperature, which is close to the virial temperature,  $\sim 10^{12}$  K near the compact object. As a consequence, nuclei with energies  $>10$  MeV per nucleon are abundant and Li production via  $\alpha - \alpha$  spallation of CNO nuclei by neutrons is possible inside the ADAF region (Yi & Narayan 1997). Li production is also possible on the surface of the secondary star (Guessoum & Kazanas 1999; Fujimoto et al. 2008). Given that neutrons are relatively easy to produce in ADAFs either via  $p - \alpha$  or  $\alpha - \alpha$  reactions and a large fraction are produced with sufficient energy that they do not interact with nuclei through the Coulomb interactions and so escape from the gravitational potential of the compact object (Guessoum & Kazanas 1990). The neutrons ejected from the hot ADAF are then intercepted by the secondary star and interact with CNO nuclei through spallation to produce Li on the star’s surface (Guessoum & Kazanas 1999). Indeed, model predictions are in good agreement with the observed values in quiescent X-ray binaries (Fujimoto et al. 2008).

In binary MSPs, in principle a hot, geometrically thick accretion flow (beyond the light cylinder radius,  $R_{\text{lc}}$ ) with low ( $\sim 10^{-4}$ ) Eddington accretion rates exist similar to the quiescent X-ray binaries. The pulsar magnetosphere remains active in the disc-state and the accretion disc is truncated at a few light cylinder radii ( $R_{\text{lc}} \sim 80$  km) away from the pulsar (Papitto et al. 2019; Veledina et al. 2019). Given that the pulsar wind is active in gamma-rays and also irradiates the disc, the ion temperature of inner accretion flow is an unknown quantity. However, Qiao & Liu (2021) determine the emergent spectrum arising from an ADAF region around the weakly magnetized neutron star, considering the radiative coupling between the soft photons from the surface of the neutron star and the ADAF. The ion temperature at the inner edge of the disc (at a few light cylinder radii away

from the pulsar) is  $\sim 14$  MeV, which is sufficient to produce Li via CNO nuclei by neutrons inside the ADAF region in a similar way as in X-ray binaries. A fraction of Li produced in an ADAF (Yi & Narayan 1997) could be expelled via magneto-centrifugal propeller effects and transferred to the secondary star enhancing the Li abundance (Fujimoto et al. 2009). Also, neutrons expelled from the ADAF and intercepted by the secondary star can interact with CNO nuclei through spallation to produce Li on the star’s surface (Guessoum & Kazanas 1999; Fujimoto et al. 2008).

### 8.2 Spallation via high energy radiation

The detection of pulsed gamma-ray emission from a large number of MSPs by Fermi Large Area Telescope (Abdo et al. 2013) imply copious pair production. In MSPs, protons and electrons are initially extracted from the neutron star surface by the intense rotation-induced electric field and later transformed into electron-positron pairs through electromagnetic cascading (Sturrock 1971) in the MSP magnetosphere (Venter et al. 2009; Johnson et al. 2014). Some of these pairs are advected into the relativistic pulsar wind, powered by the pulsar’s rotational energy and end up as part of the highly relativistic magnetized wind emerging from the pulsar. The collision between the highly relativistic pulsar wind with the mass outflow from the secondary star produces an intrabinary shock structure (Romani & Sanchez 2016). The wind is compressed by the shock and so the wind particles are accelerated to higher energies. Non-thermal X-rays are produced from the accelerated particles in the shock region (Arons & Tavani 1993; Bogdanov et al. 2011). Pair particles energized in the shocked pulsar wind are accelerated to mildly relativistic velocities and beam synchrotron radiation in a hollow cone pattern which is observed in the X-ray band. X-ray emission modulated at the orbital periods have been observed in the black widow systems PSR B1957+20 (Huang et al. 2012), PSR J2215+5135, and PSR J2256–1024 (Gentile et al. 2014) as well as in PSR J1023+0038 (Bogdanov et al. 2011).

If sufficiently energetic, the intrabinary shock particles can produce gamma-rays via synchrotron or inverse Compton emission (Romani & Sanchez 2016; Wadiasingh et al. 2017; Kandel et al. 2019; Bednarek 2014). There is also some evidence of an additional higher GeV emission component arising from inverse Compton scattering of the secondary star’s thermal radiation off a cold ultra-relativistic pulsar wind (Wu et al. 2012). Although pulsar winds are usually modeled as pair winds, such winds may also inject ions (Arons 2003). Furthermore, the intrabinary shock can also be very efficient at accelerating particles through the Fermi first-order mechanism (Drury 1983). In particular, redbacks (in the pulsar-state) and black widow pulsars can have electron-positron pairs reaching energies of 1–10 TeV (Linares & Kachelrieß 2021) and protons with energies as high as 10–100 TeVs (Harding & Gaisser 1990). These protons from the intrabinary shock may subsequently interact with the companion star, and eventually lead to spallation of CNO nuclei producing Li as well. The intrabinary shock can also give rise to ion acceleration, where ions escaping from the pulsar polar caps as the result of thermionic emission (Arons 1992) are accelerated to high energies by the electric potential induced by pulsar rotation and then accelerated by the intrabinary shock. The interaction of these high energy ions with the CNO nuclei in the secondary star’s atmosphere via spallation can also result in an increase, but not significant amount, in the Li abundance (Luo & Protheroe 1998).

In the accretion-powered disc-state the pulsar wind is maximal at the equatorial plane and directly interacts with the accretion flow inner boundary to produce gamma-rays (Veledina et al. 2019). They

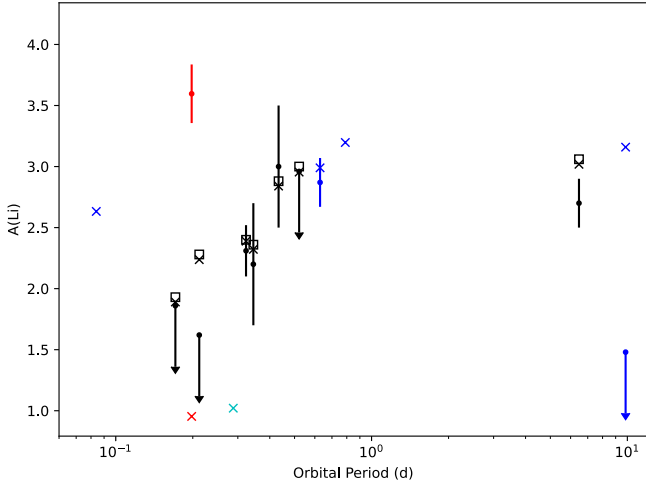


**Figure 12.** Li abundance due to neutron spallation with black hole and neutron star binaries in black and blue, respectively. PSR J1023+0038 is marked in red, and the other Galactic field tMSP PSR J1227–4853 in cyan. Dots are observed values with their corresponding error bars or upper limits. Open squares are the predicted values based on the model from Fujimoto et al. (2009), with data sourced from this paper for black hole binaries while for neutron star systems they are taken from Casares et al. (2007) and Suárez-Andrés et al. (2015b).

can also accelerate protons to energies well above 1 TeV (Papitto et al. 2014), which could subsequently lead to both very high energy gamma-rays and neutrinos (Eichler 1978). In principle, the high energy gamma-rays in MSPs can interact with the secondary star’s atmosphere to produce light elements (Eichler & Nath 1996). High energy gamma-rays or pairs impinging the secondary star’s surface cascade via bremsstrahlung pair production cycles, have photon energies above  $\sim 15$  MeV sufficient for CNO nuclei spallation to occur, leading to Li enrichment in the secondary star’s atmosphere. For particles such as cosmic-rays, Li production is also possible via spallation processes in which CNO-enriched low energy cosmic-rays accelerated in shocks interact with the ambient interstellar medium to produce Li via spallation ( $p, \alpha + C, N, O \rightarrow {}^6,7\text{Li}$ ) or fusion ( $\alpha + \alpha \rightarrow {}^6,7\text{Li}$ ; Reeves et al. 1970; Meneguzzi et al. 1971).

## 9 DISCUSSION

### 9.1 Spallation via neutrons

We consider the possibility that the unusually high Li abundance in PSR J1023+0038 is the result of spallation of CNO atoms in the upper layer of the secondary star by high-energy neutrons produced in the accretion disc as suggested in quiescent X-ray binaries (Fujimoto et al. 2008). In the following we use the methods outlined in Fujimoto et al. (2008). Assuming a mass transfer rate from the secondary star of  $4 \times 10^{13} \text{ g s}^{-1}$  (Campana et al. 2016) which corresponds to a fraction  $1.6 \times 10^{-4}$  of the Eddington rate, we estimate the neutron ejection rate from the accretion disk to be  $2 \times 10^{31} \text{ s}^{-1}$ . Using this neutron rate we can calculate the mass layer of the companion exposed to spallation and determine the production rate of Li for the system parameters of PSR J1023+0038. Assuming that the main source of Li depletion is the mass transfer from the secondary star’s surface to the accretion disc, we calculate an equilibrium Li abundance of  $A(\text{Li}) = 0.95$  dex, which is over 1000 times lower than the observed number fraction. The time-scale for Li enhancement produced from

neutron spallation is then  $\sim 194$  yr. In Fig. 12 we show the predicted and observed Li abundance for PSR J1023+0038. For comparison we show the values for the quiescent neutron star and black hole X-ray binaries (Fujimoto et al. 2008). We also show predictions for other MSPs. The main difference between the quiescent neutron star X-ray binaries and MSPs is the much lower accretion rate in the latter, which results in a lower neutron ejection rate and hence lower Li number fraction.

It should be noted that the parameters that can be modified to reconcile the predicted equilibrium abundance with observations are limited. Quantities such as cross-sections, orbital separation and companion size are only expected to vary by order unity. The equilibrium abundance varies directly with both the mass transfer rate and CNO number fraction, and inversely proportionally with the hydrogen number fraction. Despite the fact that the secondary star should overall be hydrogen-poor and CNO-rich, their linear dependence and the presence of hydrogen lines in the spectrum implies that the photosphere must retain a somewhat normal hydrogen fraction. It is not feasible for a combination of the hydrogen and CNO number densities to yield the observed Li abundance. Likewise, increasing the mass transfer rate to match the observed Li abundance would bring it to the Eddington rate, which is in direct tension with the low X-ray luminosity of the system. It therefore appears that spallation by neutrons emitted by the accretion disc is not a viable scenario to enrich the secondary star’s surface with Li in PSR J1023+0038.

### 9.2 Spallation via protons

An alternative Li production mechanism is through the spallation of CNO nuclei by protons. Such protons can be accelerated through the pulsar wind and efficiently interact with the companion star’s atmosphere. Also, protons arising from the companion star’s wind can also be accelerated in the intrabinary shock (Harding & Gaisser 1990). While precise details of the exact energy distribution and number density of protons in the pulsar wind is still an open question, it appears realistic to assume that acceleration to Lorentz factors of a few, if not higher, and proton densities of order  $n_{\text{GJ}}$ , the fiducial Goldreich-Julian density (Goldreich & Julian 1969). Recent particle-in-cell simulations have for instance demonstrated the proton outflow from the pulsar wind is largely equatorial in structure, mostly independent of the pair production efficiency and has a current density approximately decreasing with the square of the distance (Guépin et al. 2020).

Under these assumption, we can estimate the Li abundance using a similar procedure as the one employed in Section 9.1, but adopting p-p scattering as the main opacity source controlling the mass of the atmosphere exposed to proton bombardment and using the appropriate cross section for the proton spallation on CNO nuclei. For the p-p cross-section we adopt an approximate average of  $\sigma_{\text{pp}} \sim 40$  mbarn in the few tens of MeV to a few GeV range (Particle Data Group et al. 2020). Larger than a 100 MeV, the spallation cross section of p onto CNO (for the combined  ${}^6\text{Li}$  and  ${}^7\text{Li}$  isotopes) averages to around 33 mbarn (Read & Viola 1984). We calculate a proton ejection rate of  $\sim 10^{34} \text{ s}^{-1}$  for a typical MSP magnetic field and spin period. This is higher than the neutron ejection rate as the neutron production rate in the disc is driven by destruction of He, while proton production comes directly from the pulsar’s wind. Taking mass-loss (feeding the disc in the disc-state and the outgassing material creating radio eclipses in the pulsar-state) to be  $\sim 10^{-13} \text{ M}_{\odot} \text{ yr}^{-1}$  as the main depletion source (as we did for the neutron spallation case), we determine an equilibrium abundance  $A(\text{Li}) = 4.45$  dex. This value is therefore compatible with the observed measurement without requiring much

fine tuning. Furthermore, the enhancement time-scale, 600 yr, implies that equilibrium quickly settles. Thus we conclude that proton spallation is a viable mechanism.

### 9.3 Spallation via gamma-rays

An alternative option is that Li is produced via the photospallation mechanism. Eichler & Nath (1996) studied the spallation process on the surface of the secondary star induced by the gamma-ray photons from a pulsar wind, which becomes significant at energies  $\geq 15$  MeV. They found that the photodisintegration of  $^{12}\text{C}$ , even when affecting a relatively small fraction of the available atoms, produced a significant increase of lighter elements abundances, in particular B, Be and Li. The exact amount of light elements kept in the secondary star's surface depends on different parameters such as the evaporation rate and impinging flux due to the pulsar wind, the mixing depth, the size of the secondary star and the age of the system. A full calculation is beyond the scope of this paper, but we can make some estimates of the expected Li abundance. In the extreme case of total spallation of all available  $^{12}\text{C}$  nuclei, the Li abundance of a companion star would be enhanced up to  $A(\text{Li}) \sim 6.8$  for Solar  $[\text{C}/\text{H}]$  abundance (see equation 3 in Boyd & Fencl 1991). A more conservative case can be estimated if the mass-loss rate determines the exposure time of the atoms to the gamma-ray flux (i.e. considering there is no convective mixing). We assume a canonical evaporation/mass-loss rate of  $\sim 10^{13} \text{ g s}^{-1}$ , a Roche lobe filling secondary star radius of  $\sim 0.4 R_{\odot}$  determined from the system parameters of PSR J1023+0038 and a 0.3 percent efficiency in converting spin-down luminosity into 20 MeV photons, estimated from the shocked pulsar wind model proposed to explain the UV to GeV gamma-ray spectral energy distribution of PSR J1023+0038 (Takata et al. 2014). This results in  $A(\text{Li}) \sim 4.8$ , which can be regarded as an upper limit as further inclusion of the effects of a convective layer would diminish the final Li abundance.

Photospallation of heavier elements than  $^{12}\text{C}$  is expected to be less significant than the former, as their energy-weighted cross-sections are  $\sim 80$  times smaller (Boyd et al. 1989). If photospallation were the primary cause for the observed  $^{16}\text{O}$  deficit in PSR J1023+0038 spectrum, then the much more efficient photospallation of C would end up destroying all C atoms available on the surface of the secondary star (both intrinsic and proceeding from  $^{16}\text{O}$ ). The resultant Li production would then also increase accordingly, generating abundances over  $A(\text{Li}) \geq 6.5$ . This is at odds with the observations, and would in principle disfavour photospallation as the main culprit for the under-abundant  $^{16}\text{O}$ . We nevertheless note that our knowledge of the photospallation effects on atoms heavier than  $^{12}\text{C}$  is still limited, and therefore we cannot discard further resonances or production channels that would modify the final measured abundances.

In light of the previous scenarios, we conclude that spallation using high-energy gamma-rays or relativistic protons in the pulsar wind are the most likely mechanism to actively create Li at this stage of PSR J1023+0038's evolution, which would allow for a steady state abundance to be reached at the observed level despite the depletion via mass-loss in both accretion- and rotation-powered states. The main puzzle to reconcile is the under-abundant  $^{16}\text{O}$ , which perhaps can be attributed to a fine tuning of the CNO fraction during evolution or from other factors connected to the SN explosion or neutron spallation. It is interesting to note that  $^{12}\text{C}$  tends to plummet right around the phase of binary evolution connected to redbacks ( $\sim 0.2\text{--}0.5 M_{\odot}$ ), which means that the production of Li via photospallation or protons might only occur during a certain window of the binary evolution and thus, especially in black widow systems, no Li overabundance might be present.

### 9.4 Lithium preservation/depletion

Once Li has been deposited or created in the atmosphere of the secondary star it can be destroyed or preserved by various processes. We observe a high Li abundance in both the pulsar- and disc-states (see Fig. 5), which suggests that once Li is created, the destruction time-scale is sufficiently slow that Li is essentially preserved in the secondary star.

Episodes spent in the accretion-powered state act as a Li sink due to the fact that Li-rich matter is pulled away from the surface of the star via Roche lobe overflow at a faster rate than it can be produced via neutron spallation or other mechanisms, keeping it in equilibrium. Mass transfer feeding the disc is an efficient source of Li depletion. The time-scale for Li enhancement/depletion (see Section 9.1) only depends on the mass exposed to the spallation projectile bombardment and the mass-loss rate when the latter is the dominant sink source which typically amounts a few hundred years. Furthermore, it should also be noted that in the rotation-powered pulsar-state, the secondary star is observed to loose mass via an outgassing causing radio eclipses at a typical rate (see, e.g. Polzin et al. 2020) commensurate to the implied mass accretion rate in the disc-state.

Convection overshooting that mixes Li-rich material from the bottom of the convection zone to regions hot enough for it to be destroyed by nuclear reactions should occur on much larger time-scales of  $\sim 10^{7\text{--}9}$  yr (see Yi & Narayan 1997, and references within). Numerical simulations of an irradiated stellar surface comparable to that of a redback such as PSR J1023+0038 shows that a boundary layer forms under the photosphere and keeps it largely isolated from the large convective layer underneath, therefore limiting the convective mixing that can take place (Zilles et al. 2020). Furthermore, rotation plays a key role in limiting the Li depletion process (Maccarone et al. 2005) such that the Li we observe in PSR J1023+0038 most likely represents the time-averaged value over its recent history.

Indeed, the rather quick destruction Li time-scales via mass-loss ( $\sim$  tens of years) means that to explain the observed enhanced Li, it needs to be created continuously otherwise it will vanish quickly compared to the evolution time of MSPs. One corollary from this is that in 'older' spider systems the surface CNO abundance might gradually deplete and impede the regeneration of Li, thus making its abundance gradually decline. The details of this, however, would critically depend on the precise distribution of CNO inside the stars.

## CONCLUSIONS

We use high-resolution optical spectroscopy of the binary millisecond pulsar to determine the chemical abundances of the secondary star in PSR J1023+0038 which appears to be tightly controlled by a combination of the rate of angular momentum loss and the initial conditions of the binary.

- We determine a metallicity of  $[\text{Fe}/\text{H}] = 0.48 \pm 0.04$  which is higher than the Solar value and measure element abundances in the secondary star that are different compared to the secondary stars in X-ray binaries and stars in the Solar neighbourhood. Compared to the Galactic trends of stars in the Solar neighbourhood with similar Fe content the  $[\text{Si}/\text{Fe}]$  abundance is consistent, the  $[\text{Ca}/\text{Fe}]$ ,  $[\text{Al}/\text{Fe}]$  and  $[\text{Ni}/\text{Fe}]$  abundances are higher and the  $[\text{O}/\text{Fe}]$  abundance appears to be under-abundant.

- We compare the observed element abundances with the model predictions from different supernova scenarios, where matter that has been processed in the supernova is captured by the secondary star



leading to abundance anomalies, and binary stellar evolution models. We find that the spherical and aspherical supernova models with low mass cuts ( $<1.49 M_{\odot}$ ) qualitatively agree with the observations but we cannot reconcile the O and Al observed abundances. The high element abundances derived in PSR J1023+0038, in particular the high content in Fe-peak elements, support the formation of a neutron star in a SN and so argues against accretion induced collapse formation.

- We perform simulations with the binary stellar evolution code MESA and find that the O abundance at the surface of the secondary star appears to be tightly controlled by a combination rate of angular momentum loss and the initial conditions of the binary. In the case of PSR J1023+0038 where we observe hydrogen in the optical spectrum, efficient angular momentum loss must be at play. Under these conditions hydrogen is still present, and we find that the observed underabundant O is not due to the chemical anomalies associated with the CNO cycle.

- We observe Li in both the pulsar- and disc-state spectrum. Using the uncontaminated (emission line free) pulsar-state spectrum we determine the Li abundance to be  $A(\text{Li}) = 3.66 \pm 0.20$ , which is higher than the cosmic value and what is observed in young Population I stars. This provides unambiguous evidence for fresh Li production. The most likely explanation for the enhanced Li is the interaction of high-energy gamma-rays or relativistic protons in the pulsar wind with the CNO nuclei in the secondary star's atmosphere via spallation which can lead to substantial Li enrichment in the secondary star's atmosphere. The rather quick destruction time-scales over a few hundred years via mass-loss implies that the observed enhanced Li, requires continuous production in the secondary star rather than enrichment through a past event such as the supernova explosion. As most spider pulsars possess energetic winds and are prolific gamma-ray emitters, we would expect higher-than usual Li abundances to be found in other systems as well, though a gradual decay is possible as the CNO mass fraction near the surface might evolve.

## ACKNOWLEDGEMENTS

TS acknowledges acknowledges financial support from the Spanish Ministry of Science and Innovation (MICINN) project PID2020-114822GB-I00. JIGH acknowledges financial support from the Spanish Ministry of Science and Innovation (MICINN) project PID2020-117493GB-I00, and also from the Spanish MICINN under 2013 Ramón y Cajal program RYC-2013-14875. RPB and MRK acknowledge support of the European Research Council, under the European Union's Horizon 2020 research and innovation program (grant agreement No. 715051; Spiders). MRK. acknowledges funding from Irish Research Council in the form of a Government of Ireland Postdoctoral Fellowship (GOIPD/2021/670: Invisible Monsters). DMS acknowledges the Fondo Europeo de Desarrollo Regional (FEDER) and the Canary Islands government for the financial support received in the form of a grant with number PROID2020010104. ML acknowledges funding from the European Research Council (ERC) under the European Union's Horizon 2020 research and innovation programme (grant agreement No. 101002352). This work has made use of the VALD database, operated at Uppsala University, the Institute of Astronomy RAS in Moscow, and the University of Vienna. This paper makes use of data obtained from the Isaac Newton Group Archive which is maintained as part of the CASU Astronomical Data Centre at the Institute of Astronomy, Cambridge. Based on data obtained from the ESO Science Archive Facility. We gratefully acknowledge the use the MOLLY software package developed by Tom Marsh and

the PYTHON packages: MATPLOTLIB (Hunter 2007), NUMPY (van der Walt et al. 2011) and EMCEE (Foreman-Mackey et al. 2013),

Facilities: WHT (ISIS), VLT (X-SHOOTER)

## DATA AVAILABILITY

The WHT data are publicly available at the ING Archive (<http://casu.ast.cam.ac.uk/casuadc/ingarch/>). The VLT data are publicly available at the ESO Archive (<http://archive.eso.org/>).

## References

- Abdo A. A., et al., 2013, *ApJS*, **208**, 17
- Adibekyan V. Z., Sousa S. G., Santos N. C., Delgado Mena E., González Hernández J. I., Israelian G., Mayor M., Khachatryan G., 2012, *A&A*, **545**, A32
- Al-Naimiy H. M., 1978, *Ap&SS*, **53**, 181
- Alpar M. A., Cheng A. F., Ruderman M. A., Shaham J., 1982, *Nature*, **300**, 728
- Ambrosino F., et al., 2017, *Nature Astronomy*, **1**, 854
- Anders E., Grevesse N., 1989, *Geochimica Cosmochimica Acta*, **53**, 197
- Archibald A. M., et al., 2009, *Science*, **324**, 1411
- Archibald A. M., Kaspi V. M., Hessels J. W. T., Stappers B., Janssen G., Lyne A., 2013, arXiv e-prints, p. arXiv:1311.5161
- Archibald A. M., et al., 2015, *ApJ*, **807**, 62
- Arons J., 1992, *ApJ*, **388**, 561
- Arons J., 2003, *ApJ*, **589**, 871
- Arons J., Tavani M., 1993, *ApJ*, **403**, 249
- Asplund M., Grevesse N., Sauval A. J., Scott P., 2009, *ARA&A*, **47**, 481
- Bagnulo S., Jehin E., Ledoux C., Cabanac R., Melo C., Gilmozzi R., ESO Paranal Science Operations Team 2003, *The Messenger*, **114**, 10
- Barrado D., et al., 2016, *A&A*, **596**, A113
- Bassa C. G., et al., 2014, *MNRAS*, **441**, 1825
- Bednarek W., 2014, *A&A*, **561**, A116
- Benvenuto O. G., De Vito M. A., Horvath J. E., 2014, *ApJ*, **786**, L7
- Bhattacharya D., van den Heuvel E. P. J., 1991, *Phys. Rep.*, **203**, 1
- Blaauw A., 1961, *Bull. Astron. Inst. Netherlands*, **15**, 265
- Boersma J., 1961, *Bull. Astron. Inst. Netherlands*, **15**, 291
- Bogdanov S., Archibald A. M., Hessels J. W. T., Kaspi V. M., Lorimer D., McLaughlin M. A., Ransom S. M., Stairs I. H., 2011, *ApJ*, **742**, 97
- Bogdanov S., Patruno A., Archibald A. M., Bassa C., Hessels J. W. T., Janssen G. H., Stappers B. W., 2014, *ApJ*, **789**, 40
- Bogdanov S., et al., 2015, *ApJ*, **806**, 148
- Boyd R. N., Fencel H. S., 1991, *ApJ*, **373**, 84
- Boyd R. N., Ferland G. J., Schramm D. N., 1989, *ApJ*, **336**, L1
- Bressan A., Marigo P., Girardi L., Salasnich B., Dal Cero C., Rubele S., Nanni A., 2012, *MNRAS*, **427**, 127
- Breton R. P., et al., 2013, *ApJ*, **769**, 108
- Brown G. E., Lee C. H., Wijers R. A. M. J., Lee H. K., Israelian G., Bethe H. A., 2000, *New Astron.*, **5**, 191
- Brown G. E., Heger A., Langer N., Lee C. H., Wellstein S., Bethe H. A., 2001, *New Astron.*, **6**, 457
- Brown W. R., Kilic M., Allende Prieto C., Gianninas A., Kenyon S. J., 2013, *ApJ*, **769**, 66
- Büning A., Ritter H., 2004, *A&A*, **423**, 281
- Campana S., Di Salvo T., 2018, in Rezzolla L., Pizzochero P., Jones D. I., Rea N., Vignaia I., eds, *Astrophysics and Space Science Library* Vol. 457, *Astrophysics and Space Science Library*, p. 149 (arXiv:1804.03422), doi:10.1007/978-3-319-97616-7\_4
- Campana S., Coti Zelati F., Papitto A., Rea N., Torres D. F., Baglio M. C., D'Avanzo P., 2016, *A&A*, **594**, A31
- Casares J., Bonifácio P., González Hernández J. I., Molero P., Zoccali M., 2007, *A&A*, **470**, 1033
- Casares J., González Hernández J. I., Israelian G., Rebolo R., 2010, *MNRAS*, **401**, 2517

- Charbonnel C., Primas F., 2005, *A&A*, **442**, 961
- Chen H.-L., Chen X., Tauris T. M., Han Z., 2013, *ApJ*, **775**, 27
- Clayton D. D., 1983, Principles of stellar evolution and nucleosynthesis. University of Chicago Press
- Cummings J. D., Deliyannis C. P., Maderak R. M., Steinhauer A., 2017, *AJ*, **153**, 128
- Cyburtt R. H., Fields B. D., Olive K. A., 2008, *J. Cosmology Astropart. Phys.*, **2008**, 012
- D'Amico N., Lyne A. G., Manchester R. N., Possenti A., Camilo F., 2001, *ApJ*, **548**, L171
- Dahm S. E., 2015, *ApJ*, **813**, 108
- Drury L. O., 1983, *Reports on Progress in Physics*, **46**, 973
- Ecuivillon A., Israelian G., Santos N. C., Shchukina N. G., Mayor M., Rebolo R., 2006, *A&A*, **445**, 633
- Eggleton P. P., 1983, *ApJ*, **268**, 368
- Eichler D., 1978, *Nature*, **275**, 725
- Eichler D., Nath B. B., 1996, *ApJ*, **458**, 275
- Ergma E., Sarna M. J., 2001, *A&A*, **374**, 195
- Ergma E., Sarna M. J., 2003, *A&A*, **399**, 237
- Ferrario L., Wickramasinghe D., 2007, *MNRAS*, **375**, 1009
- Ferraro F. R., Possenti A., D'Amico N., Sabbi E., 2001, *ApJ*, **561**, L93
- Foreman-Mackey D., Hogg D. W., Lang D., Goodman J., 2013, *PASP*, **125**, 306
- Franciosini E., Tognelli E., Degl'Innocenti S., Prada Moroni P. G., Randich S., 2020, *Mem. Soc. Astron. Italiana*, **91**, 80
- Fu X., et al., 2018, *A&A*, **610**, A38
- Fujimoto S.-i., Matsuba R., Arai K., 2008, *ApJ*, **673**, L51
- Fujimoto S., Matsuba R., Arai K., 2009, in Kawai N., Mihara T., Kohama M., Suzuki M., eds, *Astrophysics with All-Sky X-Ray Observations*. p. 152
- Gaia Collaboration Brown A. G. A., Vallenari A., Prusti T., de Bruijne J. H. J., Babusiaux C., Biermann M., 2020, arXiv e-prints, p. arXiv:2012.01533
- Gentile P. A., et al., 2014, *ApJ*, **783**, 69
- Goldreich P., Julian W. H., 1969, *ApJ*, **157**, 869
- González Hernández J. I., Rebolo R., Israelian G., Casares J., Maeder A., Meynet G., 2004, *ApJ*, **609**, 988
- González Hernández J. I., Rebolo R., Israelian G., Casares J., Maeda K., Bonifacio P., Molaro P., 2005, *ApJ*, **630**, 495
- González Hernández J. I., Rebolo R., Israelian G., Harlaftis E. T., Filippenko A. V., Chornock R., 2006, *ApJ*, **644**, L49
- González Hernández J. I., Rebolo R., Israelian G., 2008a, *A&A*, **478**, 203
- González Hernández J. I., Rebolo R., Israelian G., 2008b, *A&A*, **478**, 203
- González Hernández J. I., Rebolo R., Israelian G., Filippenko A. V., Chornock R., Tominaga N., Umeda H., Nomoto K., 2008c, *ApJ*, **679**, 732
- González Hernández J. I., Casares J., Rebolo R., Israelian G., Filippenko A. V., Chornock R., 2011, *ApJ*, **738**, 95
- Gonzalez G., Carlson M. K., Tobin R. W., 2010, *MNRAS*, **403**, 1368
- Gray D. F., 1992, *The observation and analysis of stellar photospheres..* Cambridge University Press
- Grevesse N., Noels A., Sauval A. J., 1996, in Holt S. S., Sonneborn G., eds, *Astronomical Society of the Pacific Conference Series Vol. 99, Cosmic Abundances*. p. 117
- Guépin C., Cerutti B., Kotera K., 2020, *A&A*, **635**, A138
- Guessoum N., Kazanas D., 1990, *ApJ*, **358**, 525
- Guessoum N., Kazanas D., 1999, *ApJ*, **512**, 332
- Harding A. K., Gaisser T. K., 1990, *ApJ*, **358**, 561
- Hernanz M., Jose J., Coc A., Isern J., 1996, *ApJ*, **465**, L27
- Huang R. H. H., Kong A. K. H., Takata J., Hui C. Y., Lin L. C. C., Cheng K. S., 2012, *ApJ*, **760**, 92
- Hunter J. D., 2007, *Computing in Science & Engineering*, **9**, 90
- Hurley J. R., Tout C. A., Wickramasinghe D. T., Ferrario L., Kiel P. D., 2010, *MNRAS*, **402**, 1437
- Israelian G., Rebolo R., Basri G., Casares J., Martín E. L., 1999a, *Nature*, **401**, 142
- Israelian G., Rebolo R., Basri G., Casares J., Martín E. L., 1999b, *Nature*, **401**, 142
- Jia K., Li X.-D., 2015, *ApJ*, **814**, 74
- Johnson T. J., et al., 2014, *ApJS*, **213**, 6
- Kandel D., Romani R. W., An H., 2019, *ApJ*, **879**, 73
- Kennedy M., Garnavich P., Callanan P., Szkody P., Littlefield C., Pogge R., 2015, *ApJ*, **815**, 131
- Kennedy M. R., Clark C. J., Voisin G., Breton R. P., 2018, *MNRAS*, **477**, 1120
- Kennedy M. R., et al., 2022, arXiv e-prints, p. arXiv:2202.05111
- Koch A., Lind K., Rich R. M., 2011, *ApJ*, **738**, L29
- Kupfer T., Steeghs D., Groot P. J., Marsh T. R., Nelemans G., Roelofs G. H. A., 2016, *MNRAS*, **457**, 1828
- Kupka F. G., Ryabchikova T. A., Piskunov N. E., Stempels H. C., Weiss W. W., 2000, *Baltic Astronomy*, **9**, 590
- Kurucz R., 1993, ATLAS9 Stellar Atmosphere Programs and 2 km/s grid. Kurucz CD-ROM No. 13. Cambridge, 13
- Kurucz R. L., Furenlid I., Brault J., Testerman L., 1984, *Solar flux atlas from 296 to 1300 nm*. ESO
- Lim B., Sung H., Kim J. S., Bessell M. S., Hwang N., Park B.-G., 2016, *ApJ*, **831**, 116
- Linares M., 2014, *ApJ*, **795**, 72
- Linares M., Kachelrieß M., 2021, *J. Cosmology Astropart. Phys.*, **2021**, 030
- Luo Q., Protheroe R. J., 1998, in Chan K. L., Cheng K. S., Singh H. P., eds, *Astronomical Society of the Pacific Conference Series Vol. 138, 1997 Pacific Rim Conference on Stellar Astrophysics*. p. 229
- Maccarone T. J., Jonker P. G., Sills A. I., 2005, *A&A*, **436**, 671
- Maeda K., Nakamura T., Nomoto K., Mazzali P. A., Patat F., Hachisu I., 2002, *ApJ*, **565**, 405
- Maeda K., Mazzali P. A., Nomoto K., 2006, *ApJ*, **645**, 1331
- Martin E. L., Rebolo R., Casares J., Charles P. A., 1992, *Nature*, **358**, 129
- Martin E. L., Casares J., Charles P. A., Rebolo R., 1995, *A&A*, **303**, 785
- Martin E. L., Lodieu N., Pavlenko Y., Béjar V. J. S., 2018, *ApJ*, **856**, 40
- Mathews G. J., et al., 2020, *Mem. Soc. Astron. Italiana*, **91**, 29
- Matteucci F., Grisoni V., Romano D., 2020, *Mem. Soc. Astron. Italiana*, **91**, 128
- Meléndez J., Casagrande L., Ramírez I., Asplund M., Schuster W. J., 2010, *A&A*, **515**, L3
- Meneguzzi M., Audouze J., Reeves H., 1971, *A&A*, **15**, 337
- Menou K., Esin A. A., Narayan R., Garcia M. R., Lasota J.-P., McClintock J. E., 1999, *ApJ*, **520**, 276
- Michaud G., 1986, *ApJ*, **302**, 650
- Mucciarelli A., Salaris M., Lanzoni B., Pallanca C., Dalessandro E., Ferraro F. R., 2013, *ApJ*, **772**, L27
- Narayan R., Yi I., 1995, *ApJ*, **452**, 710
- Narayan R., McClintock J. E., Yi I., 1996, *ApJ*, **457**, 821
- Nelemans G., Tauris T. M., van den Heuvel E. P. J., 1999, *A&A*, **352**, L87
- Nelemans G., Yungelson L. R., van der Sluys M. V., Tout C. A., 2010, *MNRAS*, **401**, 1347
- Nomoto K., Kondo Y., 1991, *ApJ*, **367**, L19
- Nomoto K., Tanaka M., Tominaga N., Maeda K., 2010, *New Astron. Rev.*, **54**, 191
- Orosz J. A., van Kerkwijk M. H., 2003, *A&A*, **397**, 237
- Orosz J. A., et al., 2001, *ApJ*, **555**, 489
- Papitto A., et al., 2013, *Nature*, **501**, 517
- Papitto A., Torres D. F., Li J., 2014, *MNRAS*, **438**, 2105
- Papitto A., et al., 2019, *ApJ*, **882**, 104
- Particle Data Group et al., 2020, *Progress of Theoretical and Experimental Physics*, **2020**, 083C01
- Pasquini L., Koch A., Smiljanic R., Bonifacio P., Modigliani A., 2014, *A&A*, **563**, A3
- Patruno A., et al., 2014, *ApJ*, **781**, L3
- Paxton B., et al., 2013, *ApJS*, **208**, 4
- Paxton B., et al., 2019, *ApJS*, **243**, 10
- Pecaut M. J., Mamajek E. E., 2013, *ApJS*, **208**, 9
- Pinsonneault M., 1997, *ARA&A*, **35**, 557
- Pinsonneault M. H., Deliyannis C. P., Demarque P., 1992, *ApJS*, **78**, 179
- Pitrou C., Coc A., Uzan J.-P., Vangioni E., 2018, *Phys. Rep.*, **754**, 1
- Podsiadlowski P., Nomoto K., Maeda K., Nakamura T., Mazzali P., Schmidt B., 2002, *ApJ*, **567**, 491
- Polzin E. J., et al., 2018, *MNRAS*, **476**, 1968
- Polzin E. J., Breton R. P., Bhattacharyya B., Scholte D., Sobey C., Stappers B. W., 2020, *MNRAS*, **494**, 2948

- Portegies Zwart S. F., Verbunt F., Ergma E., 1997, *A&A*, **321**, 207
- Prantzos N., 2012, *A&A*, **542**, A67
- Prantzos N., de Laverny P., Guiglion G., Recio-Blanco A., Worley C. C., 2017, *A&A*, **606**, A132
- Qiao E., Liu B. F., 2021, *MNRAS*,
- Radhakrishnan V., Srinivasan G., 1982, *Current Science*, **51**, 1096
- Read S. M., Viola V. E. J., 1984, *Atomic Data and Nuclear Data Tables*, **31**, 359
- Reeves H., Fowler W. A., Hoyle F., 1970, *Nature*, **226**, 727
- Reid M. J., et al., 2009, *ApJ*, **700**, 137
- Roberts M. S. E., 2013, in van Leeuwen J., ed., *IAU Symposium Vol. 291, Neutron Stars and Pulsars: Challenges and Opportunities after 80 years.* pp 127–132 ([arXiv:1210.6903](https://arxiv.org/abs/1210.6903)), doi:10.1017/S174392131202337X
- Romani R. W., Sanchez N., 2016, *ApJ*, **828**, 7
- Ruderman M., Shaham J., Tavani M., 1989, *ApJ*, **336**, 507
- Sabbi E., Gratton R. G., Bragaglia A., Ferraro F. R., Possenti A., Camilo F., D’Amico N., 2003, *A&A*, **412**, 829
- Sadakane K., et al., 2006, *PASJ*, **58**, 595
- Schroeder J., Halpern J., 2014, *ApJ*, **793**, 78
- Shahbaz T., 1998, *MNRAS*, **298**, 153
- Shahbaz T., et al., 2015, *MNRAS*, **453**, 3461
- Shahbaz T., Linares M., Breton R. P., 2017, *MNRAS*, **472**, 4287
- Shahbaz T., Linares M., Rodríguez-Gil P., Casares J., 2019, *MNRAS*, **488**, 198
- Smedley S. L., Tout C. A., Ferrario L., Wickramasinghe D. T., 2015, *MNRAS*, **446**, 2540
- Snedden C., Bean J., Ivans I., Lucatello S., Sobeck J., 2012, MOOG: LTE line analysis and spectrum synthesis (ascl:1202.009)
- Spite F., Spite M., 1982, *A&A*, **115**, 357
- Stappers B. W., et al., 2014, *ApJ*, **790**, 39
- Strader J., et al., 2019, *ApJ*, **872**, 42
- Stringer J. G., et al., 2021, arXiv e-prints, p. [arXiv:2107.11306](https://arxiv.org/abs/2107.11306)
- Sturrock P. A., 1971, *ApJ*, **164**, 529
- Suárez-Andrés L., González Hernández J. I., Israelian G., Casares J., Reboló R., 2015a, *MNRAS*, **447**, 2261
- Suárez-Andrés L., González Hernández J. I., Israelian G., Casares J., Reboló R., 2015b, *MNRAS*, **447**, 2261
- Takata J., et al., 2014, *ApJ*, **785**, 131
- Tauris T. M., van den Heuvel E. P. J., 2006, *Formation and evolution of compact stellar X-ray sources.* Cambridge University Press, pp 623–665
- Thorstensen J. R., Armstrong E., 2005, *AJ*, **130**, 759
- Umeda H., Nomoto K., 2003, *Nature*, **422**, 871
- Van K. X., Ivanova N., 2019, *ApJ*, **886**, L31
- Van K. X., Ivanova N., Heinke C. O., 2019, *MNRAS*, **483**, 5595
- Veledina A., Nättälä J., Beloborodov A. M., 2019, *ApJ*, **884**, 144
- Venter C., Harding A. K., Guillemot L., 2009, *ApJ*, **707**, 800
- Voisin G., Kennedy M. R., Breton R. P., Clark C. J., Mata-Sánchez D., 2020, *MNRAS*, **499**, 1758
- Wadiasingh Z., Harding A. K., Venter C., Böttcher M., Baring M. G., 2017, *ApJ*, **839**, 80
- Wang E. X., Nordlander T., Asplund M., Amarsi A. M., Lind K., Zhou Y., 2021, *MNRAS*, **500**, 2159
- Wenger M., et al., 2000, *A&AS*, **143**, 9
- Woosley S. E., Weaver T. A., 1995, *ApJS*, **101**, 181
- Woosley S. E., Hartmann D. H., Hoffman R. D., Haxton W. C., 1990, *ApJ*, **356**, 272
- Woudt P. A., Warner B., Pretorius M. L., 2004, *MNRAS*, **351**, 1015
- Wu E. M. H., Takata J., Cheng K. S., Huang R. H. H., Hui C. Y., Kong A. K. H., Tam P. H. T., Wu J. H. K., 2012, *ApJ*, **761**, 181
- Xiong D. R., Deng L., 2009, *MNRAS*, **395**, 2013
- Yi I., Narayan R., 1997, *ApJ*, **486**, 363
- Zilles A., Kotera K., Rohrmann R., Althaus L., 2020, *MNRAS*, **492**, 1579
- van den Heuvel E. P. J., Habets G. M. H. J., 1984, *Nature*, **309**, 598
- van der Walt S., Colbert S. C., Varoquaux G., 2011, *Computing in Science Engineering*, **13**, 22

This paper has been typeset from a  $\text{\TeX}/\text{\LaTeX}$  file prepared by the author.